UNIVERSIDAD DE CANTABRIA

FACULTAD DE CIENCIAS

Estudio estructural del multiferroico $CaMn_7O_{12}$ bajo presión mediante cálculos de Teoría del Funcional de la Densidad

(Structural study of multiferroic $CaMn_7O_{12}$ under pressure by means of Density Functional Theory calculations)

Trabajo de fin de grado para acceder al

grado en Física

Autor: Jaime Garrido Aldea

Correo: jaime.garrido@alumnos.unican.es

Directora: Virginia Monteseguro Padrón

Junio 2022

Agradecimientos (Acknowledgements)

Comienzo dando las gracias a mi tutora Virginia. Tengo que darle las gracias no solo por su gran ayuda para este trabajo, también por haber conseguido que lo disfrute de principio a fin. Creo sinceramente que no podría haber disfrutado más la realización de esta memoria. Es mérito suyo por haber dado en el clavo con un tema y un enfoque que pueda disfrutar. Me alegra poder acabar el grado en física disfrutando así.

Quería seguir dando las gracias a Javier Ruiz Fuertes. Durante 2021-2022 he crecido muchísimo, y es en gran parte gracias a él, por su labor como profesor y mentor y por darme oportunidades para crecer como científico. Este texto tampoco existiría si no hubiera sido por Javier.

Estos 5 años en la universidad han sido extremadamente duros, pero he tenido la suerte de poder compartirlos con Sergio, Paula y Alba. He podido acudir a ellos siempre que lo he necesitado y he aprendido infinidad con ellos, tanto a nivel académico como a nivel personal. No podía haber coincidido con mejores compañeros. Voy a echar mucho de menos los ratos entre aulas, así que espero poder compensarlo fuera de ellas.

Convivir con promociones que no son la propia es raro, sobre todo cuando la mayor parte de la tuya ha abandonado la facultad. Tengo que agradecer a Laura, Elsa y Leku que acabaran con esa sensación extraña. No han podido hacerme sentir más integrado.

Mi amigo Miguel es la persona con más sentido crítico que he conocido. Me alegro muchísimo de que el grado me permitiera conocerlo. No solo quiero agradecer su amistad, también que haya conseguido que disfrute muchísimo cada asignatura que hemos tenido en común. Todos los momentos en los que he recordado por qué me gusta la ciencia han sido con Miguel al lado.

La mitad de este trabajo se realizó desde Madrid. Allí me resultó imprescindible Eloy, con quien puedo compartir mucho más que mi interés por la ciencia. No olvidaré ni los entrenos, ni las charlas de biomecánica ni el camino hacia la catorce.

Por último, tengo que dar las gracias a mi padre, mi madre y mi hermano. Ellos siempre se han esforzado para que yo solo tenga que dejarme la piel estudiando. No me podían haber dado más facilidades. Sin su ayuda, no me estaría despidiendo de la Universidad de Cantabria.

Resumen

$CaMn_7O_{12}$ es un semiconductor que en condiciones ambiente presenta la peculiaridad de que sus átomos de manganeso actúan con distintas valencias. Este hecho hace que ciertos átomos de Mn sufran el efecto Jahn-Teller y se encuentren en una coordinación de octahedro comprimido. Se ha encontrado experimentalmente que este compuesto presenta una transición de fase con reordenamiento de carga al aumentar la presión. En esta transición de fase, el efecto Jahn-Teller juega un papel importante. En este trabajo se ha obtenido un *parámetro de Hubbard* U capaz de describir las propiedades electrónicas del $CaMn_7O_{12}$ con cálculos de teoría del funcional de la densidad. Con dicho parámetro, se han obtenido propiedades estructurales del compuesto en función de la presión, lo que permite analizar en detalle la transición de fase y el rol que juega el efecto Jahn-Teller en ella. Los resultados tanto electrónicos como estructurales son consistentes con trabajos ya publicados.

Palabras clave: calcio, manganeso, oxígeno, Teoría del Funcional de la Densidad, efecto Jahn-Teller, *parámetro de Hubbard*, transición de fase, estructura.

Abstract

$CaMn_7O_{12}$ is a semiconductor with the peculiarity that at ambient conditions, its manganese atoms act with different valences. This fact makes certain Mn atoms suffer the Jahn-Teller effect, being in a distorted octahedron coordination. It was found experimentally that this compound undergoes a charge-ordering phase transition under pressure. The Jahn-Teller effect plays an important role in this phase transition. In this work, a U *Hubbard parameter* capable of describing the electronic properties of $CaMn_7O_{12}$ with Density Functional Theory calculations has been obtained. With that parameter, structural properties of the compound have been obtained under pressure. This allows to analyze with detail the phase transition and the role the Jahn-Teller effect plays on it. Results, both electronic and structural, are consistent with published work.

Keywords: calcium, manganese, oxygen, Density Functional Theory, Jahn-Teller effect, *Hubbard parameter*, phase transition, structure.

Contents

Each of us is carving a stone, erecting a column, or cutting a piece of stained glass in the construction of something much bigger than ourselves.

Adrienne Clarkson

Chapter 1

Introduction

1.1 Why are we here?

The first acid test for the Schrödinger equation was the problem of the hydrogen atom: one proton and one electron. The simplicity of the system allowed to find explicit solutions for the wavefunction of the electron. The huge success of the solutions in terms of their concordance with experimental results is greatly convincing about the fact that the Schrödinger equation is indeed a good computational tool to obtain the properties of quantum-mechanical systems.

The sad part of the story is that solving this equation explicitly or numerically is out of reach in many cases, including most of those who involve several interacting particles. Fortunately, some geniuses found an alternative way to approach these kind of problems, giving birth to Density Functional Theory, which basically formulates interacting particles problems in terms of non-interacting particles problems.

Density Functional Theory was the first step into designing specialized software capable of obtaining the properties of quantum-mechanical systems via *ab initio*-type calculations. One of the many programs available to achieve such a thing is VASP (Vienna Ab initio Simulation Package) [1], the one used in this work.

Our system of interest is the compound $CaMn_7O_{12}$, a semiconductor that presents some interesting features such that being multiferroic, Jahn-Teller affected, having manganese acting with different valences...[2]. This compound undergoes a charge-ordering phase transition under pressure in which the Jahn-Teller effect plays an important role. This transition under pressure has been studied experimentally in [2] but it is yet to be studied by means of *ab initio*-type calculations.

We will check how the U *Hubbard parameter* (a parameter used in a certain type of Density Functional calculations) heavily influences both the electronic structure and the local structure. Finally, we will see how a good description of the electronic properties leads to a good description of the structure.

Therefore, we will firstly obtain the optimal U *Hubbard parameter* that reproduces the electronic properties of the compound. Afterwards, we will obtain the structural properties (both at short and long range) as a function of pressure and we will study the phase transition for the optimal U.

1.2 How to read this text

This text aims to be understood by all readers with a degree-level knowledge of physics. However, all the contents of a typical physics degree are assumed to be known by the reader, in particular, those related with basic solid state physics. Chapter 2 offers a deep enough theoretical introduction to understand Density Functional Theory, the process and fundamentals of this work. Chapter 3 explains the details necessary to reproduce all calculations. Chapter 4 explains briefly the experimental

results that motivate and serve as context for this work. Chapter 5 contains the important results, with the less relevant being left for chapter 6. Finally, chapter 7 offers the conclusions and the closure of this text.

Claims that cannot be tested, assertions immune to disproof are veridically worthless, whatever value they may have in inspiring us or exciting our sense of wonder.

Carl Sagan

Chapter 2

Theoretical backround

2.1 Introduction to Density Functional Theory (DFT)

In this section, the fundamentals of Density Functional Theory (DFT) will be introduced. The aim of the section is to give the reader a deep enough introduction to the topic so that the computational method is understood at a conceptual level. We will follow the steps of [3][Part II]. Any additional references will be explicitly written.

2.1.1 Defining the general problem we want to solve

In order to unveil the properties of any system at a quantum scale, one must solve the Schrödinger equation. Let us consider a system of electrons and nuclei. The Hamiltonian governing such a system is [3][Page 52], [4][Page 77]:

$$\begin{aligned}\hat{H} = &-\frac{\hbar^2}{2m_e}\sum_i \nabla_i^2 + \sum_{i,I}\frac{Z_I e^2}{|\mathbf{r}_i - \mathbf{R}_I|} + \frac{1}{2}\sum_{i\neq j}\frac{e^2}{|\mathbf{r}_i - \mathbf{r}_j|} \\ &-\sum_I \frac{\hbar^2}{2M_I}\nabla_I^2 + \frac{1}{2}\sum_{I\neq J}\frac{Z_I Z_J e^2}{|\mathbf{R}_I - \mathbf{R}_J|},\end{aligned} \tag{2.1}$$

Where m_e is the electron mass, e its charge, $Z_I e$ is the charge of nuclei I,M_I its mass,$\mathbf{R}_I$ its coordinates and $\mathbf{r}_i$ the coordinates of the electron i. Note that we are omitting a $1/4\pi\epsilon_0$ dividing factor in those terms regarding potential energy.

Solving the Schrödinger equations means solving:

$$\hat{H}\Psi = E\Psi \tag{2.2}$$

Where Ψ is the wavefunction of the whole system and E its energy.

Solving the equation with such a complicated hamiltonian is a task so difficult that it is not worth the effort. It is better to approach the problem by other means.

Firstly, we know that nuclei are way heavier than electrons. It is therefore reasonable to assume that nuclei velocities are very small in comparison to electron velocities. Hence, we can neglect the nuclei kinetic energy term in the previous hamiltonian:

$$\hat{H} = -\frac{\hbar^2}{2m_e}\sum_i \nabla_i^2 + \sum_{i,I}\frac{Z_I e^2}{|\mathbf{r}_i - \mathbf{R}_I|} + \frac{1}{2}\sum_{i\neq j}\frac{e^2}{|\mathbf{r}_i - \mathbf{r}_j|} + \frac{1}{2}\sum_{I\neq J}\frac{Z_I Z_J e^2}{|\mathbf{R}_I - \mathbf{R}_J|}, \tag{2.3}$$

This approximation is called the Born-Oppenheimer approximation. A good mathematical description can be found at [3][Appendix C], but for this text, it is enough to understand the fact that we are considering the nuclei to be frozen. The wavefunction we will get is a wavefunction corresponding to a certain fixed configuration of the nuclei.

From now on, we will use Hartree atomic units, i.e $\hbar = m_e = e = 4\pi/\epsilon_0 = 1$. With these units, the previous hamiltonian can be decomposed in different terms, starting with the kinetic energy of the electrons:

$$\hat{T} = \sum_i -\frac{1}{2}\nabla_i^2 \tag{2.4}$$

The potential energy due to the interaction between nuclei and electrons:

$$\hat{V}_{\text{ext}} = \sum_{i,I} V_I\left(|\mathbf{r}_i - \mathbf{R}_I|\right) = \sum_{i,I} \frac{Z_I e^2}{|\mathbf{r}_i - \mathbf{R}_I|} \tag{2.5}$$

The potential energy due to the interaction between electrons:

$$\hat{V}_{\text{int}} = \frac{1}{2}\sum_{i\neq j} \frac{1}{|\mathbf{r}_i - \mathbf{r}_j|} \tag{2.6}$$

And finally, the potential energy due to the interaction between nuclei:

$$E_{II} = \frac{1}{2}\sum_{I\neq J} \frac{Z_I Z_J e^2}{|\mathbf{R}_I - \mathbf{R}_J|} \tag{2.7}$$

With the previous notation, the hamiltonian can be expressed as follows:

$$\hat{H} = \hat{T} + \hat{V}_{\text{ext}} + \hat{V}_{\text{int}} + E_{II} \tag{2.8}$$

So, as it was stated at the begining of this section, to obtain the properties of the system under study, we have to solve the Schrödinger equation. In our case, the hamiltonian we have to use is the one in equation (2.8). Now the problem is that we have no means to solve the equation. For now, we can only ask ourselves: how can we move on? Do we have any way to sort this issue?

2.1.2 The Hohenberg-Kohn theorems

Let us begin this section with the following question: what if there is a way to obtain all the properties we want without solving the Schrödinger equation with the hamiltonian in (2.8)?

The results we are going to expose here are definitely game changing, and alter completely the *modus operandi* one should follow. These results are the Hohenberg-Kohn theorems, first published in 1964 [5]. Although the original formulations and proofs are in [5], we are going to present it the way is done in [3][Page 122]. The proofs are not included here for the sake of concision.

Theorem 1 *For any system of interacting particles in an external potential $V_{ext}(\mathbf{r})$, the potential $V_{ext}(\mathbf{r})$ is determined uniquely, except for a constant, by the ground state particle density $n_0(\mathbf{r})$.*

Note that the problem we are trying to solve (remember: solving the Schrödinger equation with the hamiltonian in (2.8)) is about a system of interacting particles (the electrons interact between them) and are under the influence of an external potential (the potential created by the nuclei). Therefore, the situation we are facing satisfies the hypothesis of the theorem. Now we proceed with an important corollary.

Corollary 1 *$n_0(\mathbf{r})$ determines $V_{ext}(\mathbf{r})$, and $V_{ext}(\mathbf{r})$ determines the hamiltonian. Equivalently, the hamiltonian determines the wavefunctions, and the wavefunctions determine the properties of the system. As a result, the ground state particle density, $n_0(\mathbf{r})$, determines all the properties of the system.*

The previous corollary suggests a different way to solve our problem. If we had the ground state particle density and a method to obtain all magnitudes with it, we would had everything. But note that these results do not give you any hint on how to do so.

Figure 2.1 shows how these two results add a twist to the way we would proceed before.

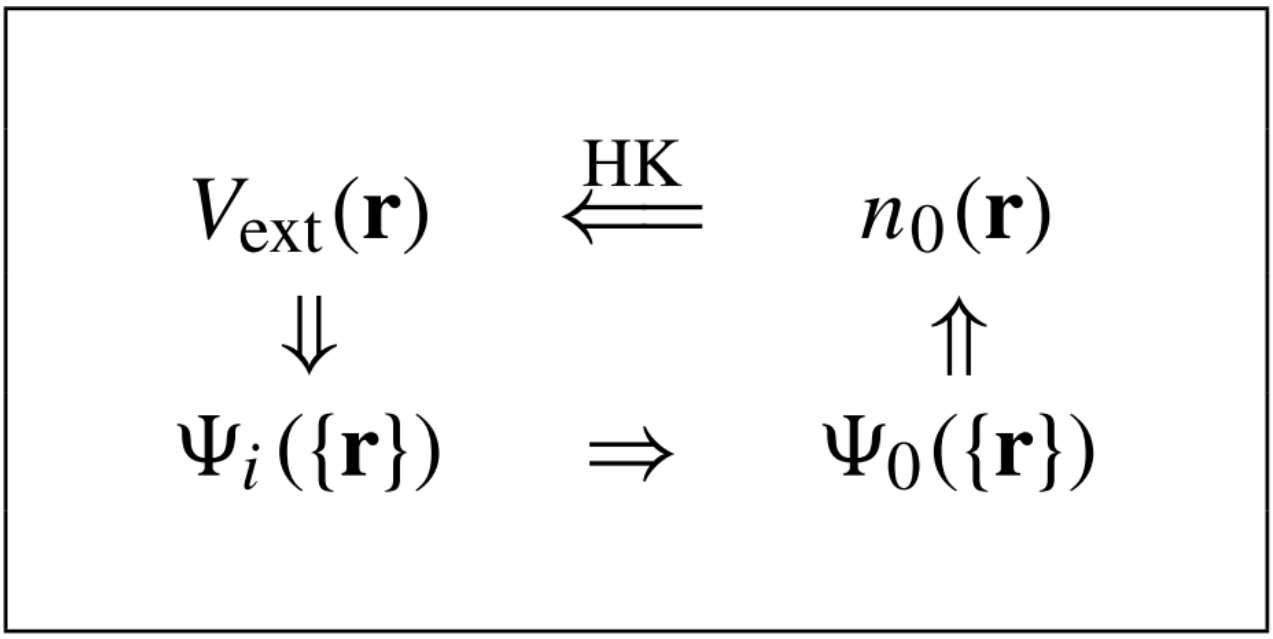

Figure 2.1: This scheme illustrates the contribution of theorem 1. The usual procedure was solving the Schrödinger equation with a known potential. Then obtaining all possible states (in particular, the ground state) and then, the ground state particle density. With theorem 1, we know that with the ground state particle density we can get the external potential and the circle is complete. The figure has been extracted from [3][Page 122].

The two previous results claim that there should be a way to obtain all properties from the ground state particle density. They do not say a thing about how to do it. The following theorem solves partially this issue for the energy of the system and the ground state particle density.

Theorem 2 *A universal functional for the energy $E[n]$ in terms of the density $n(\mathbf{r})$ can be defined, valid for any external potential $V_{ext}(\mathbf{r})$. For any particular $V_{ext}(\mathbf{r})$, the exact ground state energy of the system is the global minimum value of this functional, and the density $n(\mathbf{r})$ that minimizes the functional is the exact ground state density $n_0(\mathbf{r})$.*

The weakness of the theorem is that it does not give any clue about how to build such a functional. From the theorem, we get the obvious corrollary:

Corollary 2 *If $E[n]$ is given, the ground state energy can be obtained by minimizing it and $n_0(\mathbf{r})$ is the function n that minimizes it. Hence the functional $E[n]$ alone is sufficient to determine the exact ground state energy and density.*

Although we are not writing the proof, we write an important step of it. From theorem 1, we know that all properties of the system are determined by the ground state density. As a result, all kind of energies must be a functional of the density, including the total energy [3][Page 124]:

$$\begin{aligned} E_{\text{HK}}[n] &= T[n] + E_{\text{int}}[n] + \int \mathrm{d}^3 r V_{\text{ext}}(\mathbf{r}) n(\mathbf{r}) + E_{II} \\ &\equiv F_{\text{HK}}[n] + \int \mathrm{d}^3 r V_{\text{ext}}(\mathbf{r}) n(\mathbf{r}) + E_{II} \end{aligned} \tag{2.9}$$

Where $F_{\text{HK}}[n]$ is:

$$F_{\text{HK}}[n] = T[n] + E_{\text{int}}[n] \tag{2.10}$$

In these expressions, the subindex HK refers to Hohenberg-Kohn. $E_{\text{int}}[n]$ is the interaction energy between electrons. This term includes repulsion between electrons and the exchange energy. The term with the integral includes the potential energy of the electrons due to the presence of an external potential. The last term E_{II} is the already defined potential energy due to the interaction between nuclei. Note that this term does not include a dependence on n. The reason for this is that in our

context, nuclei are fixed, and therefore, this value is a constant.

After arriving at this point, our desire is to have an explicit version of $F_{\text{HK}}[n]$ in order to obtain the total energy and the ground state particle density of the system. Sad news are we do not have such an explicit functional.

Even though we have no explicit form for the previous functionals, these expressions will come on handy, as it is explained in the following section.

2.2 The Kohn-Sahm approach

In 1965, Kohn and Sahm proposed a different approach to sort out the issue of solving the Schrödinger equation with a hamiltonian of a system of interacting particles [6]. Their idea was to substitute the original interacting particles problem by an easier problem of non interacting particles with a special hamiltonian. Note that hamiltonians of non-interacting particles systems are way easier to solve that those with interacting particles. Before going on, let us write the assumptions in which their approach rests [3][Page 134]:

- The ground state particle density of the interacting system is equal to the ground state particle density of some non-interacting system.
- The auxiliary hamiltonian is chosen to have the usual kinetic operator and an effective local potential $V^{\sigma}_{\text{eff}}(\mathbf{r})$ acting on an electron of spin σ at point $\mathbf{r}$.

$$
\begin{array}{ccccccc}
V_{\text{ext}}(\mathbf{r}) & \overset{\text{HK}}{\Longleftarrow} & n_0(\mathbf{r}) & \overset{\text{KS}}{\Longleftrightarrow} & n_0(\mathbf{r}) & \overset{\text{HK}_0}{\Longrightarrow} & V_{\text{KS}}(\mathbf{r}) \\
\Downarrow & & \Uparrow & & \Uparrow & & \Downarrow \\
\Psi_i(\{\mathbf{r}\}) & \Rightarrow & \Psi_0(\{\mathbf{r}\}) & & \psi_{i=1,N_e}(\mathbf{r}) & \Leftarrow & \psi_i(\mathbf{r})
\end{array}
$$

Figure 2.2: On the right, the Kohn-Sham auxiliary system. The arrow with HK_0 represents the Hohenberg-Kohn theorem applied to the auxilary system of non-interacting particles. The arrow labeled KS represents the connection between the auxilary system and the real system. Since every two points are connected, thanks to the HK theorems, solving for the auxiliary system determines all properties of the real many-body system. The figure has been extracted from [3][Page 137].

Leaving aside whether or not these assumptions are reasonable, the fact is that their approach has proved to be really successful for many problems.

With these assumptions, we would have a hamiltonian with the following form[1]:

$$\hat{H}^{\sigma}_{\text{aux}} = -\frac{1}{2}\nabla^2 + V^{\sigma}_{\text{eff}}(\mathbf{r}) \tag{2.11}$$

[1]Important remark: this is a case of a non-interacting particles system. Therefore, the solutions of the Schrödinger equation are going to represent one possible state for a single particle (one specific energy for a specific spin). In other words, the solutions do not represent the wavefunction of the whole system. The ground state of the whole system can be obtained by filling the orbitals with the lowest energies until we have N particles. A clear example can be a hidrogen-like system of N non-interacting electrons. To get the ground state, we would fill the orbitals with lowest energies until we fill N (of course, considering that each orbital can have 2 electrons, one for each spin).

Let us write the solutions of the Schrödinger equation with the previous hamiltonian as $\psi_i^\sigma(\mathbf{r})$, and ϵ_i^σ as its eigenvalues. σ represents the spin. If we consider a case of N independent particles, the ground state can be obtained by filling the spin-dependent orbitals with lowest energies until we fill a total of N. After doing so, we would have filled N^σ orbitals for each spin σ. With this notation, the particle density is:

$$n(\mathbf{r}) = \sum_\sigma n(\mathbf{r},\sigma) = \sum_\sigma \sum_{i=1}^{N^\sigma} |\psi_i^\sigma(\mathbf{r})|^2 \tag{2.12}$$

And the kinetic energy:

$$T_s = -\frac{1}{2}\sum_\sigma \sum_{i=1}^{N^\sigma} \langle \psi_i^\sigma | \nabla^2 | \psi_i^\sigma \rangle = \frac{1}{2}\sum_\sigma \sum_{i=1}^{N^\sigma} \int d^3r \, |\nabla \psi_i^\sigma(\mathbf{r})|^2 \tag{2.13}$$

Where the s as a subindex is written to clarify that it is the kinetic energy for the non-interacting particles system (The auxiliary system).

Let us define now the Hartee energy functional:

$$E_{\text{Hartree}}[n] = \frac{1}{2}\int \mathrm{d}^3r \, \mathrm{d}^3r' \frac{n(\mathbf{r})n(\mathbf{r}')}{|\mathbf{r}-\mathbf{r}'|} \tag{2.14}$$

This functional gives the potential energy due to the interaction between electrons (remember that we are working with Hartree atomic units) in the classical sense.

Now, we shall go back to the interacting particles system. Recall that the total energy could be written as a functional of the density (equation (2.9)):

$$\begin{aligned} E_{\text{HK}}[n] &= T[n] + E_{\text{int}}[n] + \int \mathrm{d}^3r V_{\text{ext}}(\mathbf{r})n(\mathbf{r}) + E_{II} \\ &\equiv F_{\text{HK}}[n] + \int \mathrm{d}^3r V_{\text{ext}}(\mathbf{r})n(\mathbf{r}) + E_{II} \end{aligned}$$

Remember that HK is just a subindex to reference the Hohenberg-Kohn theorems. The idea of Kohn and Sahm is to rewrite the previous expression the following way:

$$E_{\text{KS}}[n] = T_s[n] + \int \mathrm{d}^3r V_{\text{ext}}(\mathbf{r})n(\mathbf{r}) + E_{\text{Hartree}}[n] + E_{II} + E_{\text{xc}}[n] \tag{2.15}$$

Where the subindex KS is just a reference to the Kohn and Sahm approach. $E_{\text{xc}}[n]$ is the so called exchange-correlation functional. This functional includes the exchange energy and all the correlation effects. Note that $T[n]$ is different from $T_s[n]$ since in the auxliary system, the particles are not interacting. As a consequence, there are some effects that $T_s[n]$ is not taking into consideration. This is why we do not only need to include an exchange term but also a contribution for the correlation.

Both energies, $E_{\text{KS}}[n]$ and $E_{\text{HK}}[n]$ must be equal. If we make them equal and we solve for $E_{\text{xc}}[n]$, we obtain:

$$E_{\text{xc}}[n] = F_{\text{HK}}[n] - (T_s[n] + E_{\text{Hartree}}[n]) \tag{2.16}$$

$$E_{\text{xc}}[n] = T[n] - T_s[n] + E_{\text{int}}[n] - E_{\text{Hartree}}[n] \tag{2.17}$$

Which express mathematically the form of the exchange-correlation functional. The importance of the previous two equations will be understood in the following section.

2.3 The Kohn-Sahm equations

With equation (2.15) and after some mathematical tools (check [3][Pages 138-139] for details about the derivation), the following equations are obtained:

$$(H^{\sigma}_{\mathrm{KS}} - \varepsilon^{\sigma}_{i})\,\psi^{\sigma}_{i}(\mathbf{r}) = 0 \tag{2.18}$$

$$H^{\sigma}_{\mathrm{KS}}(\mathbf{r}) = -\frac{1}{2}\nabla^2 + V^{\sigma}_{\mathrm{KS}}(\mathbf{r}) \tag{2.19}$$

$$\begin{aligned} V^{\sigma}_{\mathrm{KS}}(\mathbf{r}) &= V_{\mathrm{ext}}(\mathbf{r}) + \frac{\delta E_{\mathrm{Hartree}}}{\delta n(\mathbf{r},\sigma)} + \frac{\delta E_{\mathrm{xc}}}{\delta n(\mathbf{r},\sigma)} \\ &= V_{\mathrm{ext}}(\mathbf{r}) + V_{\mathrm{Hartree}}\,(\mathbf{r}) + V^{\sigma}_{\mathrm{xc}}(\mathbf{r}). \end{aligned} \tag{2.20}$$

These three equations are the so called Kohn-Sahm equations. Note that equation (2.18) is a Schrödinger-like equation for a non-interacting particles system. Its hamiltonian depends on the particle density, which depends on the orbitals that are the solution of the equation. We have a situation in which the potential depends on the solutions but at the same time, the solutions depend on the potential. To solve this, one tries with a first trial density and a self consistent algorithm [7][Page 14]. More details of how to solve the equations will be given in section 2.5.

We can go back to the question of the importance of equations (2.16) and (2.17). Note that if we knew the exact form of $E_{\mathrm{xc}}[n]$ and the external potential, we would know $V^{\sigma}_{\mathrm{KS}}(\mathbf{r})$ and therefore, we could solve the Schrödinger-like Kohn-Sahm equation (2.18) with a self consistent algorithm. By solving that equation, we could obtain all the auxiliary system wavefunctions, then the ground state particle density of the auxliary system and its energy. The energy of the interacting particles system would be equal to that of the auxiliary system since both have the same ground state particle density (theorem 1). And all of this, with all the precision our numerical software can manage. If $E_{\mathrm{xc}}[n]$ is known exactly, the results are exact. To summarize, what we have here is an exact tool. In practice, the only errors will be a consequence of numerical errors and approximations for the effective potential.

The reality is that we do not have the exact form of the exchange-correlation functional and we have to use approximations [4][Pages 80-81]. How to face this issue and the ins and outs of solving the Kohn-Sahm equations is the goal of section 2.5.

2.4 The meaning of the Kohn-Sahm eigenstates

Recall the main idea of the Kohn-Sahm approach: replacing the original system of interacting particles by an auxiliary system of non-interacting particles with a different Hamiltonian. A logical question after this ansatz is: do the solutions for the auxilary system have a meaning? Let us try to answer that.

Now that we know the details of the Hamiltonian (equations (2.18-2.20)) we can see that despite having a Hamiltonian of non-interacting particles, the effects of the interactions between particles are implicitly considered with the different terms of equation (2.20). This could lead us to think that the Kohn-Sahm eigenstates i.e the solutions of equation (2.18) have a meaning as parts of the interacting system.

This last idea is a bit tricky. Keep in mind that we started with a system of interacting particles with a many-body wavefunction i.e a single wavefunction that describes the whole system. After all the ideas exposed in this chapter, we arrived to a system of non-interacting particles that we can describe via single-particle wavefunctions but all the interactions are somehow considered via an effective potential. So, actually, we are expressing the properties of the interacting-system in terms

of single-particle wavefunctions, in contrast with the real solution that would be a many-body wavefunction.

Regarding this, excellent clarifications are given in [8][Section 2.6]. The Kohn-Sahm eigenstates represent ficticious particles (Since they belong to the auxiliary ficticious system) but they are extremely useful to describe the properties of the system in terms of them. In fact, this ficticious particles resemble a bit their real counterparts since the effects of interaction, exchange and correlation are taken into account into the effective potential.

The success of this description will be obvious when analyzing the band structure of $CaMn_7O_{12}$ in chapter 5.

2.5 How to handle the Kohn-Sahm equations

The Kohn-Sahm equations are usually solved with a self consistent algorithm as shown in figure 2.3. Some steps require further explanation and deserve more attention. We will use these subsections to give more details about those steps.

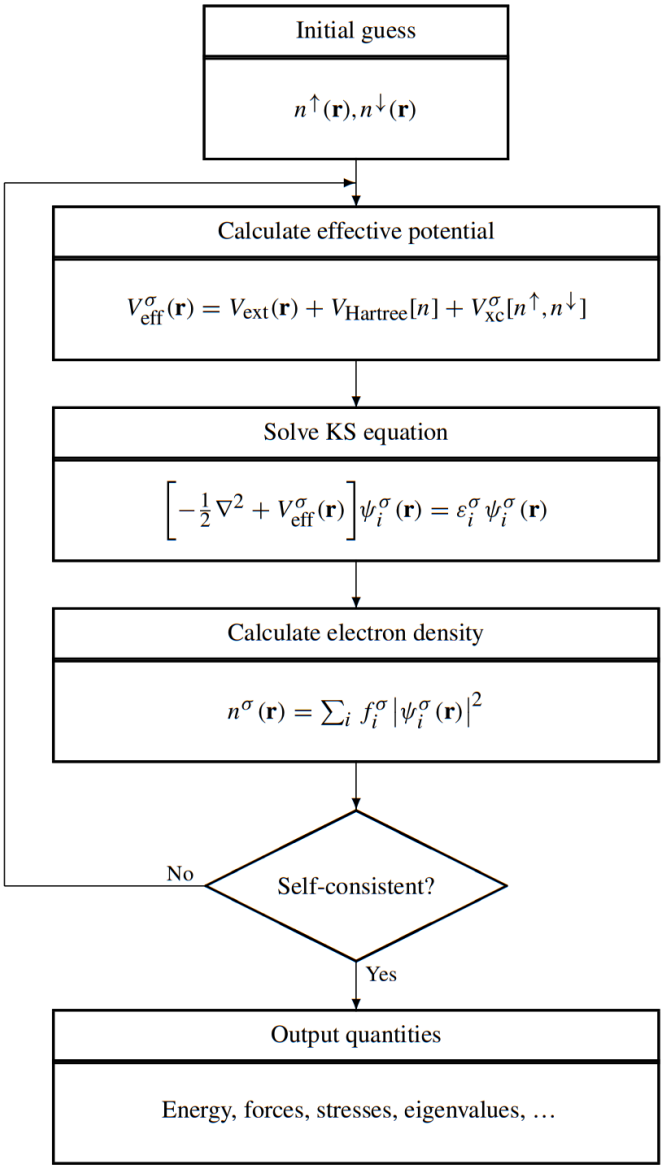

Figure 2.3: Flow chart of a self consistent algorithm to solve the Kohn-Sahm equations. The scheme has been extracted from [3][Page 173].

2.5.1 Calculation of the exchange-correlation potential

As it was said before, we have no exact form for the exchange-correlation functional and we have to go to approximations. Having an approximated functional allows us to obtain the exchange-correlation potential that appears in the Schrödinger-like Kohn-Sahm equation (2.18) and from there, move on. We are going to introduce four different approximations for the sake of learning and completeness.

Local density approximation (LDA)

First proposed in 1965 by Kohn and Sahm [6][Page 1135], this approximation consists on approximating the exchange-correlation functional as follows [7][Page 18],[9][Page 22]:

$$E_{\mathrm{xc}}^{\mathrm{LDA}}[n] = \int n(\mathbf{r})\varepsilon_{\mathrm{xc}}^{\mathrm{unif}}(n(\mathbf{r}))\mathrm{d}\mathbf{r} \tag{2.21}$$

where $\varepsilon_{\mathrm{xc}}^{\mathrm{unif}}(n)$ is the exchange-correlation energy per particle of the infinite uniform electron gas with density n.

The function $\varepsilon_{\mathrm{xc}}^{\mathrm{unif}}(n)$ has exchange and correlation contributions i.e $\varepsilon_{\mathrm{xc}}^{\mathrm{unif}}(n) = \varepsilon_{\mathrm{x}}^{\mathrm{unif}}(n) + \varepsilon_{\mathrm{c}}^{\mathrm{unif}}(n)$. The exchange energy per particle is well known analytically, but the correlation energy per particle is not. However, the correlation contribution has been numerically calculated via Monte Carlo calculations [10].

Local spin density approximation (LSDA)

The local density approximation does not take into account the spin polarization of the system. Let $n^{\uparrow}$ be the particle density for spin up particles and $n^{\downarrow}$ the particle density for spin down particles. The LSDA approximation consists on approximating the exchange correlation functional as follows [3][Page 153]:

$$\begin{aligned} E_{\mathrm{xc}}^{\mathrm{LSDA}}\left[n^{\uparrow}, n^{\downarrow}\right] &= \int \mathrm{d}^3 r n(\mathbf{r}) \epsilon_{\mathrm{xc}}^{\mathrm{unif}}\left(n^{\uparrow}(\mathbf{r}), n^{\downarrow}(\mathbf{r})\right) \\ &= \int \mathrm{d}^3 r n(\mathbf{r}) \left[\epsilon_x^{\mathrm{unif}}\left(n^{\uparrow}(\mathbf{r}), n^{\downarrow}(\mathbf{r})\right) + \epsilon_c^{\mathrm{unif}}\left(n^{\uparrow}(\mathbf{r}), n^{\downarrow}(\mathbf{r})\right)\right] \end{aligned} \tag{2.22}$$

Where $\epsilon_{\mathrm{xc}}^{\mathrm{unif}}\left(n^{\uparrow}(\mathbf{r}), n^{\downarrow}(\mathbf{r})\right)$ is the exchange-correlation energy per particle of the infinite uniform electron gas with spin up density $n^{\uparrow}(\mathbf{r})$ and spin down density $n^{\downarrow}(\mathbf{r})$. So essentially, it is analogous to the LDA approximation for spin polarized systems. The last equality of equation (2.22) follows from the division of the exchange-correlation energy per particle into an exchange contribution and a correlation contribution.

This approximation works better for systems similar to the uniform electron gas such as nearly-free electron metals.

Generalized-Gradient Approximations (GGAs)

This kind of approximations were born to take into consideration the non-uniform density of solids [7][Page 18] (Remember that the previous approximations considered a situation akin to a uniform electron gas). In order to do so, the designed exchange-correlation functional is not only a functional of the density but a functional of both density and its gradients [9][Page 24]. A general form for this functionals is [3][Page 154]:

$$E_{\mathrm{xc}}^{\mathrm{GGA}}\left[n^{\uparrow}, n^{\downarrow}\right] = \int \mathrm{d}^3 r n(\mathbf{r}) \epsilon_{\mathrm{xc}}\left(n^{\uparrow}, n^{\downarrow}, \left|\nabla n^{\uparrow}\right|, \left|\nabla n^{\downarrow}\right|, \ldots\right) \tag{2.23}$$

GGA's approximations are better than LSDAs in many cases [3][Page 153]. They work well for atoms and molecules since they describe well exchange-correlation effects on low density zones. Nevertheless, they are not good for strongly correlated systems [7][Page 19].

DFT+U approximations for the exchange-correlation functional

DFT is successful in many cases, but it fails in the description of highly correlated systems due to inability of the exchange-correlation functional to represent the many body effects. These functionals tend to overlocalize valence electrons and assign lower energies to metallic ground states. [11][Page 5].

In strongly correlated systems, the coulombic repulsion between electrons make them localized in such a way they cannot move between atoms, they can move only by hopping[2][11][Page 6].

DFT+U is a method to obtain better exchange-correlation functionals which aim for a better description of strongly correlated systems. In this context, U is the so called *Hubbard parameter*. The objective is to introduce a correction in the functional to take into consideration the strong coulombic repulsion between the very localized electrons. These kind of corrections improve the description of correlated states while keeping the same good description of valence states given by DFT. In particular, this approach serves as a good description of the d and f orbitals, which in many cases are the ones participating in the bonds and hence, they determine a lot of properties of a compound [11][Page 7]. The corrections are dependent on two parameters: U and J (both with energy units. We will omit units to work only with eV) which measure the coulomb interaction and the exchange respectively. The choice of this parameters is done semiemipirically, choosing those values that make the best agreement of a certain magnitude with experimental data [12].

Putting everything into equations, the exchange-correlation functional would be like [13][Page 4]:

$$E_{\text{DFT}+U} = E_{\text{DFT}} + E_U \tag{2.24}$$

Where E_U is the new contribution to the functional.

No more details are needed for the understanding of this work, but the interested reader can find more information on [11], [12], [13] and the references therein.

2.5.2 Approximations for the external potential: pseudopotentials

In the effective potential of the Kohn-Sahm equations (2.20), there is a contribution of the external potential acting on the system, $V_{\text{ext}}(\mathbf{r})$. This external potential is originated by the ions and acts over all electrons. The electrons that influence the most the properties of a system are those in the outer shells of the atoms i.e the valence electrons. These valence electrons interact with valence electrons of other atoms. Their interaction, their bond, determines greatly the physical and chemical properties.

The idea of a pseudopotential is to focus only on these valence electrons. Instead of considering all the electrons in our auxiliary system of non-interacting electrons, we can consider only the valence electrons. Then, core electrons do not contribute to the particle density[3] but their effect on the system is considered by means of an alternative external potential called a pseudopotential.

To sum up, pseudopotentials are effective potentials acting on valence electrons that aim to represent the effect of the nucleus and the core electrons on the valence electrons [3][Page 204]. By using them, the original problem is replaced by other with a different Hamiltonian and a different external potential. The eigenfunctions of the new hamiltonian are called pseudowavefunctions. The wavefunctions of the original Hamiltonian (the one that considers all electrons) are called all-electron wavefunctions.

Good pseudopotentials satisfy the following properties [3][Page 213]:

[2] We are referring to the quantum hopping effect.

[3] Remember that the effective potential of the Kohn-Sahm equations is a functional of the particle density. If the core electrons are not considered in the particle density, the effective potential changes. To compensate this change, the effects of the core electrons on the total energy are incorporated in the pseudopotential.

1. All-electron eigenvalues and pseudoeigenvalues agree for the chosen atomic configuration.
2. All-electron wavefunctions and pseudowavefunctions agree for values of r greater than a cutoff radius r_c.
3. The logarithmic derivatives[4] of the wavefunctions and pseudowavefunctions agree at the cutoff radius.
4. The integral of the wavefunctions and pseudowavefunctions between 0 and r_c are equal.

The usefulness of pseudopotentials is that they make calculations way faster thanks to the fact that they consider only the valence electrons. The four previous properties translate intuitively as shown in figure 2.4.

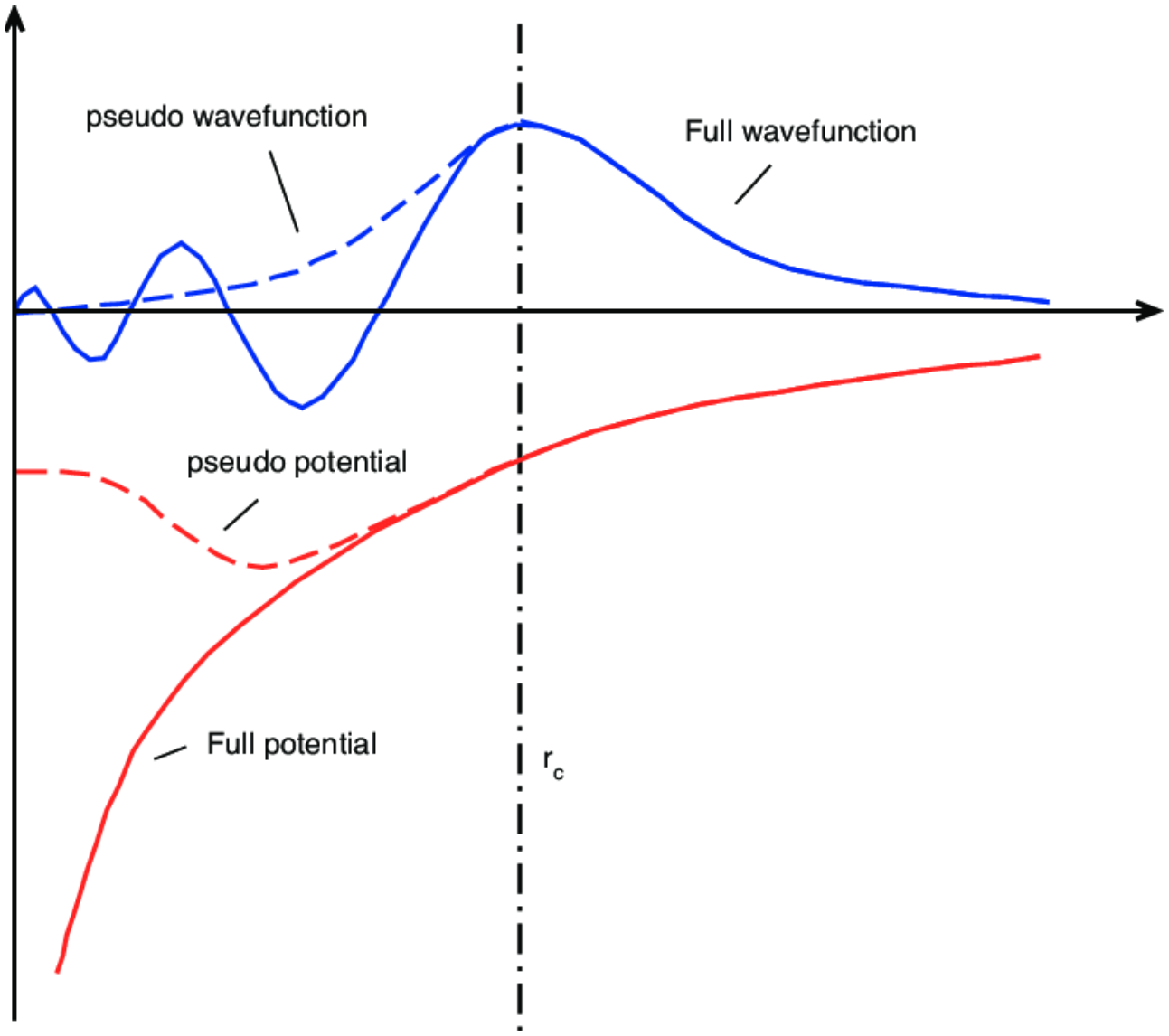

Figure 2.4: In blue: the pseudowavefunction (Dashed) and the all-electron wavefunction (Plain). In red: pseudopotential (Dashed) and full potential (Plain). The dashed black vertical line shows the cutoff radius, named r_c in the plot. The figure has been extracted from [14][Figure 4.1].

2.5.3 The PAW approach

The projector augmented wave method (PAW) serves to simplify calculations by solving an alternative Schrödinger-like equation with smooth solutions [3][Page 225]. Only the essential details will be

[4]The logarithmic derivative is defined as $D_l(\varepsilon, r) \equiv r\psi_l'(\varepsilon, r)/\psi_l(\varepsilon, r) = r\frac{\mathrm{d}}{\mathrm{d}r}\ln\psi_l(\varepsilon, r)$

given in this section. The interested reader can go to [3][Section 11.11].

The PAW approach consists on defining a smooth part of a valence wavefunction: $\tilde{\psi}_i^v(\mathbf{r})$ and a linear transformation $\psi^v = \mathcal{T}\tilde{\psi}^v$ relating the all-electron wavefunctions ψ^v and the smooth valence wavefunctions. The transformation is unity except in a sphere centered in the nucleus.

With those definitions and after some good and difficult ideas, an alternative Schrödinger-like equation for the smooth wavefunctions can be obtained:

$$\hat{H}^{\text{PKA}}\tilde{\psi}_i^v(\mathbf{r}) \equiv \left[-\frac{1}{2}\nabla^2 + \hat{V}^{\text{PKA}}\right]\tilde{\psi}_i^v(\mathbf{r}) = \varepsilon_i^v\tilde{\psi}_i^v(\mathbf{r}) \tag{2.25}$$

This new Schrödinger-like equation is easier to solve than the original one and the full wavefunction can be obtained via the transformation $\mathcal{T}$ previously defined.

2.5.4 Solutions of the Schrödinger-like equations

Bloch's theorem states that the wavefunctions of the electrons (In the one-electron frame) in a periodic crystal can be written as [7][Pages 24-25]:

$$\psi_{\mathbf{k}}(\mathbf{r}) = e^{i\mathbf{k}\cdot\mathbf{r}}u_{\mathbf{k}}(\mathbf{r}) \tag{2.26}$$

Which means that $\mathbf{k}$ is a good quantum number. $u_{\mathbf{k}}(\mathbf{r})$ is a function with the periodicity of the direct lattice, this means that if $\mathbf{R}$ is a vector of the direct lattice, $u_{\mathbf{k}}(\mathbf{r}) = u_{\mathbf{k}}(\mathbf{r}+\mathbf{R})$. Functions that satisfy this last property can be expanded as a sum of reciprocal lattice plane waves:

$$u_{\mathbf{k}}(\mathbf{r}) = \sum_{\{\mathbf{G}\}} e^{i\mathbf{G}\cdot\mathbf{r}}c_{\mathbf{k},\mathbf{G}} \tag{2.27}$$

$\{\mathbf{G}\}$ represents the set of reciprocal lattice vectors, $\mathbf{G}$, a specific reciprocal lattice vector and $c_{\mathbf{k},\mathbf{G}}$ are the coefficients of the expansion. By inserting (2.27) into (2.26), we get:

$$\psi_{\mathbf{k}}(\mathbf{r}) = \sum_{\{\mathbf{G}\}} c_{\mathbf{k},\mathbf{G}}e^{i(\mathbf{G}+\mathbf{k})\cdot\mathbf{r}} \tag{2.28}$$

As a result, we can write the one-electron wavefunctions as in equation (2.28). The coefficients $c_{\mathbf{k},\mathbf{G}}$ can be calculated by inserting equation (2.28) into a Schrödinger equation, then multypling both sides by a plane wave $e^{i\mathbf{G}\cdot\mathbf{r}}$ and then integrating in all real space.

The issue now is that (2.28) runs over an infinite number of plane waves, which is not possible to implement in numerical calculations. In practice, we need to take a finite number of terms. To do so, an energy cutoff is specified in such a way, only the plane waves with equal or less energy are considered. Mathematically, for a fixed $\mathbf{k}$ and energy cutoff E_{encut}, the sum in (2.28) is truncated to:

$$\psi_{\mathbf{k}}(\mathbf{r}) = \sum_{\{\mathbf{G}:\frac{\hbar^2|\mathbf{G}+\mathbf{k}|^2}{2m}\leq E_{encut}\}} c_{\mathbf{k},\mathbf{G}}e^{i(\mathbf{G}+\mathbf{k})\cdot\mathbf{r}} \tag{2.29}$$

Finding an appropiate energy cutoff is part of every DFT calculation.

2.6 Ionic relaxations

This work required many geometry optimizations. A geometry optimization process finds the positions of the nuclei such that the total energy is in a local minima. In a local minima, the nuclei are in equilibrium. As a result, the total force acting on each nuclei is zero (in practice, numerically zero). Nevertheless, nuclei belong to a unit cell with a specific volume and shape and therefore, the total force on each nuclei must be zero with the requirement of a certain volume and shape of the unit cell.

The shape and volume of the unit cell is determined by the stress tensor $\sigma_{\alpha\beta}$. As a result, in order to find such the equilibrium configuration, we need a method to calculate the values of the stress tensor and another one to calculate the forces acting on each atom.

The forces acting on an atom can be calculated with the Hellmann-Feynman theorem [3][Page 57]. Let $\mathbf{F}_I$ be the force acting on the nuclei I, with coordinates $\mathbf{R}_I$. The Hellman-Feynman theorem states that:

$$\mathbf{F}_I = -\frac{\partial E}{\partial \mathbf{R}_I} = -\int \mathrm{d}^3 r n(\mathbf{r}) \frac{\partial V_{\text{ext}}(\mathbf{r})}{\partial \mathbf{R}_I} - \frac{\partial E_{II}}{\partial \mathbf{R}_I} \tag{2.30}$$

Giving then an explicit way to calculate forces on the nuclei.

The components $\sigma_{\alpha\beta}$ of the stress tensor can be calculated analitically [3][Page 59]:

$$\sigma_{\alpha\beta} = -\left\langle \Psi \left| \sum_k \frac{\hbar^2}{2m_k} \nabla_{k\alpha} \nabla_{k\beta} - \frac{1}{2} \sum_{k \neq k'} \frac{(\mathbf{x}_{kk'})_\alpha (\mathbf{x}_{kk'})_\beta}{x_{kk'}} \left(\frac{\mathrm{d}}{\mathrm{d}x_{kk'}} \hat{V} \right) \right| \Psi \right\rangle \tag{2.31}$$

Where the sum over k and k' runs over all particles, both nuclei and electrons.

In this work we wanted to subject the $CaMn_7O_{12}$ system to hydrostatic pressure. Having an explicit way of calculating the components of the stress tensor serves as a way to check wether or not the pressure is hydrostatic. If the pressure is hydrostatic, the stress tensor is diagonal.

2.7 The Jahn-Teller effect

The Jahn-Teller effect is the consequence of the Jahn-Teller theorem, formulated by them in 1937 [15]: *"We shall show that stability and degeneracy are not possible simultaneously unless the molecule is a linear one"*. Although the statement refers explicitly to molecules, it also applies to complexes in solids. Our case of interest is its effect on octahedral complexes.

So now, let us take as example a Mn^{3+}- O_6 octahedron in a solid. The electronic configuration of the manganese atom is [Ar]$3d^4$. A regular octahedron belongs to the space group O_h. We already know that the O_h symmetry affecting the manganese atom leads to a shift of its energy levels, in particular, the $3d$ energy levels [16][Pages 255-260]. The $3d$ energy levels get divided into an e_g doublet with energy above the initial and a t_{2g} triplet with energy below the initial. The e_g doublet and the t_{2g} triplet are separated by an amount of energy named Δ. Depending on the value of Δ, the split orbitals are filled differently [17]. If Δ is greater than the energy required to pair two electrons, the t_{2g} is filled completely before the e_g. When Δ is less than the pairing energy, the e_g is filled before pairing the electrons in t_{2g}. Examples of these two situations are depicted in figure 2.5. Figure 2.5 up shows one and only one spin down electron. Note that this spin down electron could be placed in either the d_{yz} or the d_{xy} orbitals while maintaining the same total energy. Therefore, the state is degenerate. Similarly, figure 2.5 down has only one electron on the e_g level. This electron could be placed in the $d_{x^2-y^2}$ and the system would maintain the same energy. Therefore, the state is degenerate. The conclusion is: does not matter the value of Δ, the Mn^{3+}- O_6 octahedron is in a degenerate state. As a result, the Jahn-Teller theorem applies, the system is not stable and this degeneracy must be broken.

Degeneracy is broken by splitting the e_g and t_{2g} levels. This splitting can be done in the two different ways figure 2.6 shows [17]. In practice, the break of degeneracy translates into a distortion at the octahedron, making it elongated or compressed along its long axis.

So in the end, the Jahn-Teller effect leads to a distortion at the octahedron which leads to a lower energy configuration (more stable).

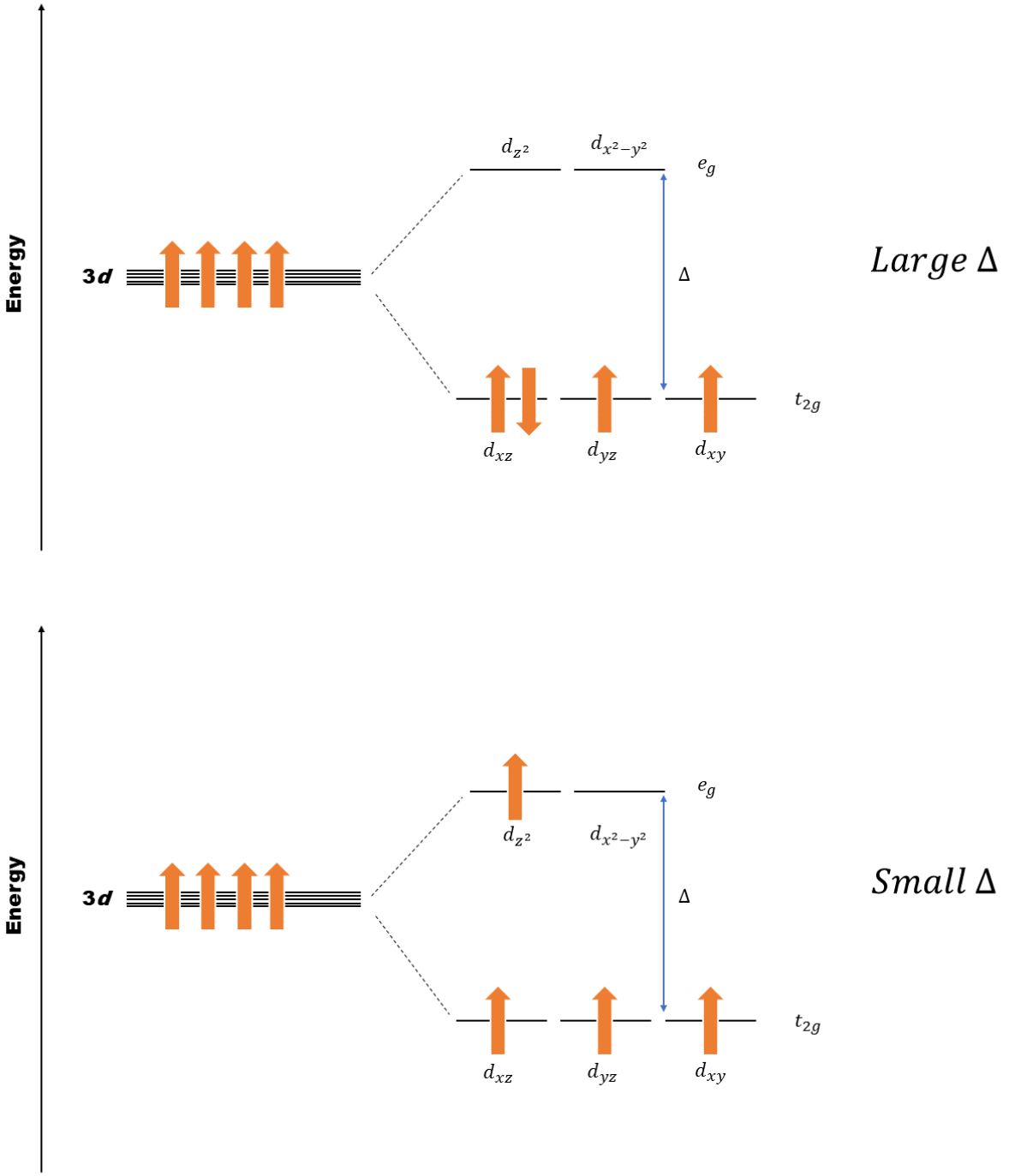

Figure 2.5: Filling of the t_{2g} and e_g depending of the value of Δ. Up: large Δ. Down: small Δ Note that in both examples, the state is degenerate. Therefore, Jahn-Teller theorem applies.

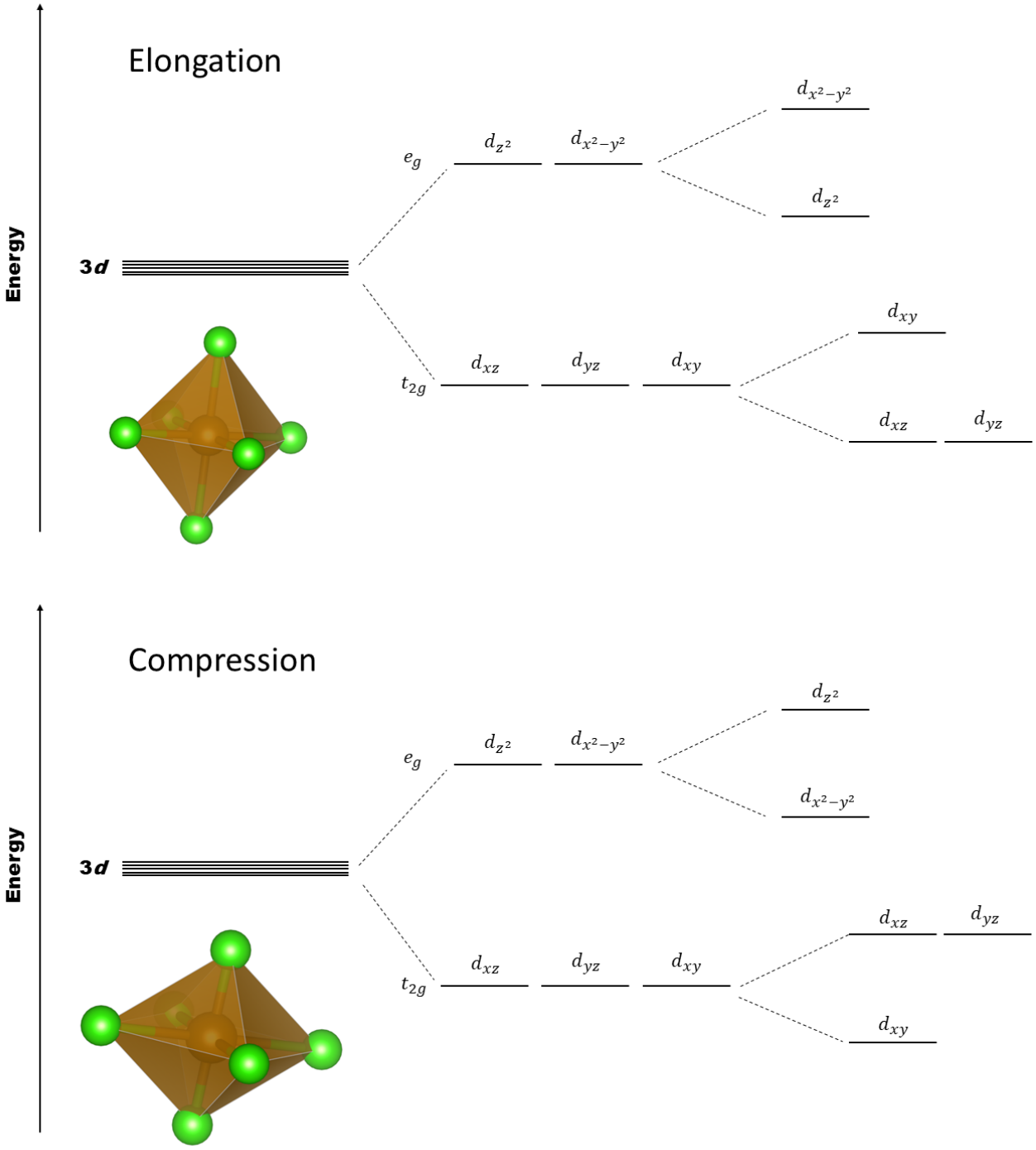

Figure 2.6: Splitting of the t_{2g} and e_g. Up: the splitting for the elongated octahedron. Down: the splitting for the compressed octahedron.

> The good thing about computers is that they do what you tell them to do. The bad news is that they do what you tell them to do.
>
> *Ted Nelson*

Chapter 3

Computational procedure with VASP

The aim of this chapter is to give details of the procedure followed to carry out all calculations and, at the same time, give a brief explanation of how VASP works. The reader unfamiliar with DFT calculations should get basic ideas so that the procedure does not seem opaque.

Remember that we aim to find the appropiate U *Hubbard parameter* and structural properties we can compare with experimental data (next chapter). Hence, we will explain briefly what was done to obtain such magnitudes.

3.1 VASP input files

VASP requires 4 input text files, with names *INCAR, POSCAR, POTCAR* and *KPOINTS*, each with a specific function:

- *INCAR*: this file is to ask for what to calculate and how.
- *POSCAR*: this file contains the geometry of the lattice (lattice vectors) and the positions of the atoms. In this work we used two different type of *POSCAR*s, one type for the low pressure phase and another one for the high pressure phase.
- *POTCAR*: contains the pseudopotential used for each atomic species and the electrons considered as valence electrons.
- *KPOINTS*: defines a mesh over the first Brillouin zone. The reciprocal space points of this mesh (*k*-points) will be those considered in the calculations.

3.2 VASP output files

VASP has many output files (way more than input files). In this text, we will introduce only the relevant ones for this context:

- *OUTCAR*: contains the resulting forces, stress tensor, pressure, cell volume internal energy...
- *CONTCAR*: it has the same format as *POSCAR*. It contains the lattice vectors and the positions of the atoms after the ionic relaxation.
- *DOSCAR*: contains the density of states and the integrated density of states.
- *CHGCAR*: contains the charge-density
- *vasprun.xml*: main output in different format. In this work, it was used to obtain the band structure.

3.3 Scheme to obtain the results

In this work, we wanted to obtain the appropiate U *Hubbard parameter* capable of correctly describing the electronic properties and structure of $CaMn_7O_{12}$.

With that being said, we can write the procedure to obtain these magnitudes:

1. Finding the energy cutoff and the size of the *k*-points mesh for proper convergence.
2. Finding the relaxed structure for the low pressure phase at 0 GPa i.e ambient pressure (for each value of the U *Hubbard parameter*).
3. Obtaining the density of states for the low pressure phase at 0 GPa with a big enough mesh (for each value of the U *Hubbard parameter*).
4. Obtaining the band structure for the low pressure phase at 0 GPa (for each value of the U *Hubbard parameter*).
5. Choosing the most appropiate value of the U *Hubbard parameter*.
6. Relaxing both phases for different values of pressure (With the U *Hubbard parameter* chosen in the previous step).

3.4 General considerations in all calculations

All calculations were performed with VASP under the Density Functional Theory approach. The PAW pseudopotential method and GGA+U were used with the functional PBEsol[18]. The J parameter was chosen to be 1.4 for all calculations as it was in [19],[20]. For Ca, $3p^6 4s^2$ electrons were considered as valence electrons. For Mn, $3p^6 3d^6 4s^1$ electrons were considered as valence electrons. For O, $2s^2 3p^4$ electrons were considered as valence electrons. Converged results were obtained by setting the energy cutoff to 500 eV. The R_k parameter (defined in the following section) was set to 40, resulting in a $8 \times 8 \times 8$ *k*-points mesh. For each volume (or pressure), the structure was relaxed after the calculation of forces on the atoms and the stress tensor. In the relaxed configuration, the forces acting on the atoms were lower than 0.005 eVÅ^{-1} and the stress tensor differed from a diagonal form in less than 0.1 GPa.

The density of states and the band structure were obtained with a dense $16 \times 16 \times 16$ mesh. The band structure was calculated along the high symmetry path $\Gamma - X|Y - \Gamma - Z|R - \Gamma - T|U - \Gamma - V$.

3.5 Finding the appropiate *k*-point mesh and energy cutoff for convergence

As it was explained in section 2.5.3, calculations require an energy cutoff in order to choose a finite number of plane waves. Besides, the *KPOINTS* file determines the number of points in the first Brillouin zone considered. What is the influence of the cutoff and the number of points on the results? For an accurate representation of a real world system, both variables should be high enough so that we get results compatible with experimental measurements. However, choosing excessively high values will delay the calculations. As a consequence, the scientist must think of a balance between precision, accuracy and computational time. The computational time has to be the minimal such that the results are obtained with the desired accuracy.

So the question now is, how do you balance the energy cutoff and the number of *k*-points so that you get accurate results? In this work, we analyzed the behaviour of the total energy as a function of both the energy cutoff and the number of *k*-points.

The first step was to take two different states for the low pressure phase (analogous for the high pressure phase) i.e at two different but very similar pressures. After doing so, the procedure was as follows:

- For a fixed number of k-points, an ionic relaxation followed by an energy calculation was performed for different values of the energy cutoff (for both pressures).
- For the highest energy cutoff considered in the previous step, an ionic relaxation followed by an energy calculation was performed for a different number of k-points (for both pressures).

Once the calculations were finished, the difference in energy between both states was analyzed as a function of both the energy cutoff and the number of k-points. Both differences should converge to a certain value for a high enough energy cutoff and a dense enough mesh.

When the number of k-points was fixed, the mesh was created with the regular mesh option with 6 subdivisions along the direction of each vector of the conventional reciprocal lattice basis. The format of the resulting *KPOINTS* file is shown in figure 3.1.

```
Automatic mesh
0                ! number of k-points = 0 ->automatic generation scheme
Gamma            ! generate a Gamma centered grid
6  6  6          ! subdivisions N_1, N_2 and N_3 along recipr. l. vectors
0. 0. 0.         ! optional shift of the mesh (s_1, s_2, s_3)
```

Figure 3.1: Format of the *KPOINTS* file for a regular mesh.

With the energy cutoff being fixed, the mesh was created with the automatic option and changing the value of the R_k parameter. The R_k parameter is a number such that [21] the mesh is:

$$\mathbf{k} = \sum_{i=1}^{3} \mathbf{b}_i \frac{n_i}{N_i} \quad \forall n_i \in [0, N_i[\tag{3.1}$$

Where $\mathbf{b}_i$ is a vector of the conventional reciprocal lattice basis and

$$N_i = \text{int}\left(\max\left(1, R_k \left|\mathbf{b}_i\right| + 0.5\right)\right) \tag{3.2}$$

The format of the resulting *KPOINTS* file is shown in figure 3.2.

```
Automatic mesh
0                ! number of k-points = 0 -> automatic generation scheme
Auto             ! fully automatic
  40             ! length (R_k)
```

Figure 3.2: Format of the *KPOINTS* file for an automatic generated mesh. The R_k parameter is specified on the last line of the file.

Once an appropiate selection of the mesh and the cutoff has been made, one can proceed with the calculations with a proper convergence guaranteed.

History is the version of past events that people have decided to agree upon.

Napoleon Bonaparte

Chapter 4

Current relevant knowledge about $CaMn_7O_{12}$

It is said that any work of art cannot be understood without its context. In a similar way, the results of this work can not be completely understood without their context. Therefore, in this chapter we will introduce some of the state of the art. The results exposed in this chapter will serve as context for the following chapters and as a source to compare the results with experimental data.

4.1 Its crystal structure at low and high pressure

$CaMn_7O_{12}$ crystallizes at ambient conditions in a rhombohedral lattice with space group $R\bar{3}$ [22][Page 14903]. Its main peculiarity is that Mn occupies three different non-equivalent positions and acts with two different valences, Mn^{3+} and Mn^{4+}. One of those positions is in a square-planar coordination (Mn1). The other two are in a octahedral coordination, but the difference in the valence makes one of them a distorted octahedron (space group D_{4h}) whereas the other one is a perfect octahedron (space group O_h) [2][Page 1]. At the distorted octahedron (Mn2) and in the square-planar coordination, the oxidation state of manganese is Mn^{3+} whereas in the regular octahedron (Mn3) is Mn^{4+}. The origin of the distortion is the Jahn-Teller effect [2][Page 1], [19][Page 4].

$CaMn_7O_{12}$ structure at ambient conditions is represented in figure 4.1. Note that the figure does not show its primitive cell. The three different non-equivalent sites for Mn are shown in figure 4.2. Note that for the compressed octahedron, there are two different distances. A distortion quenching would make the two kind of octahedra equivalent, leading to an increase in symmetry and hence, to a phase transition. There are many ways to eliminate that distortion, and applying pressure is one of those.

In [2], they show how at ambient temperature, $CaMn_7O_{12}$ undergoes a first-order charge-ordering phase transition with pressure (around 28 GPa) from a rhombohedral lattice with space group $R\bar{3}$ to a cubic lattice with space group $Im\bar{3}$. The details of the phase transition are object of the next section, but we can anticipate that the increase in pressure leads to a different charge order that ends up eliminating the distortion and the two different kinds of octahedra become equivalent. As a result in the high pressure $Im\bar{3}$ phase, there are only two different non-equivalent positions for Mn, one in a square planar coordination and another one in a perfect octahedral coordination. This situation is shown in figure 4.3.

It is important to remark that these two structures are very similar. So similar that in [2][Page 4], the X-ray diffraction refinement was convergent for the $Im\bar{3}$ phase even for pressures below the phase transition pressure.

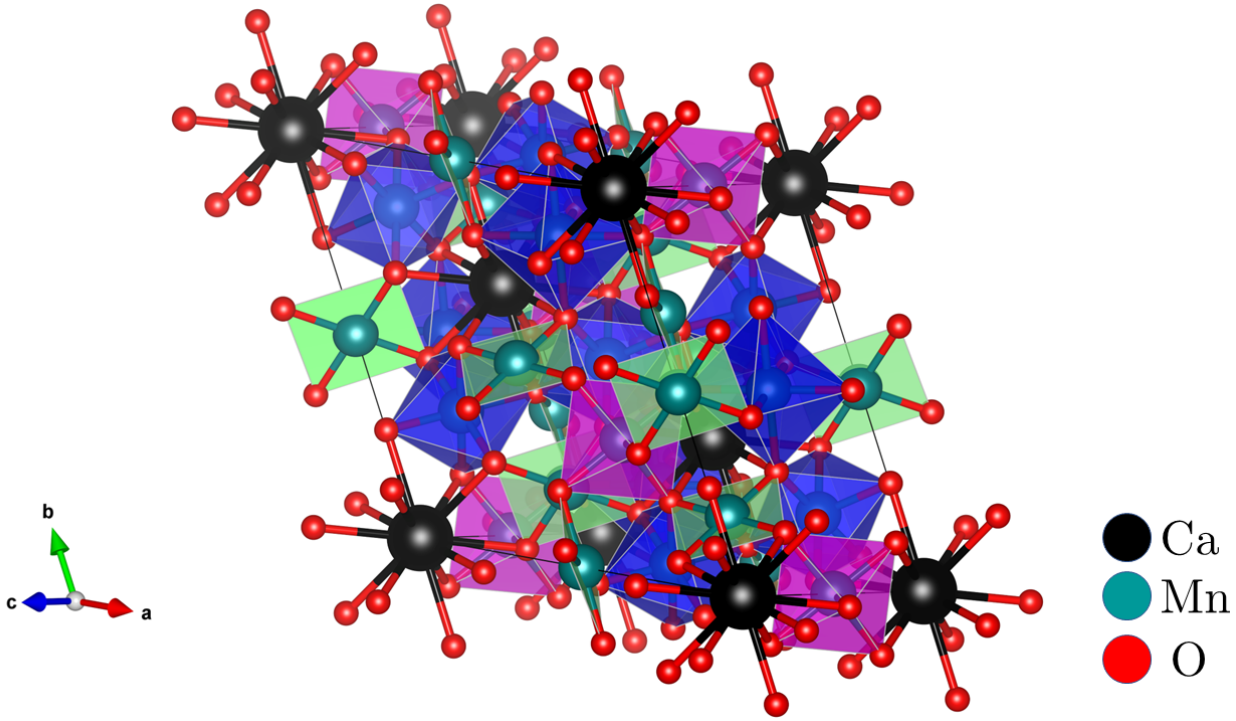

Figure 4.1: Ambient conditions crystal structure of $CaMn_7O_{12}$. Its lattice is rhombohedral type with spatial group $R\bar{3}$. Blue octahedra are those for Mn2 i.e distorted octahedra with Mn^{3+}. Pink octahedra are the regular octahedra (Mn3 with Mn^{4+}). Green squares show the square-planar coordination of Mn1.

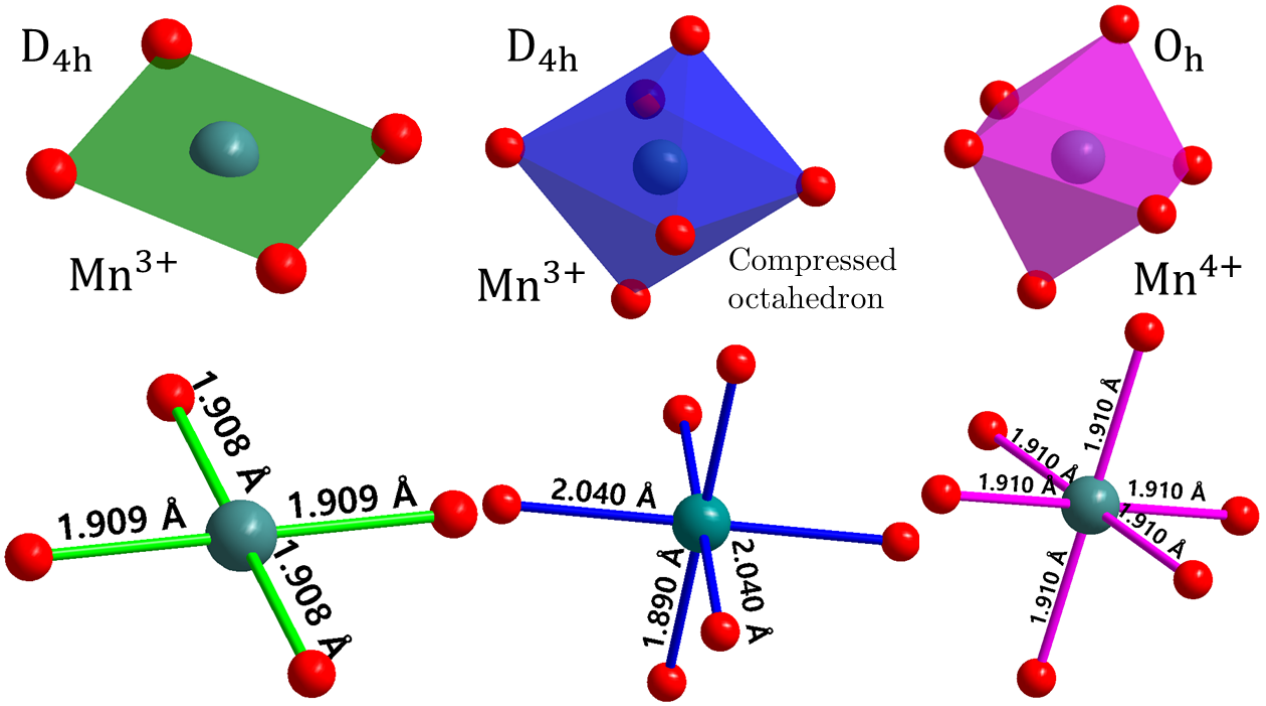

Figure 4.2: The three different positions that Mn can occupy at the low pressure $R\bar{3}$ phase of $CaMn_7O_{12}$. The distorted octahedron has 2 different distances.

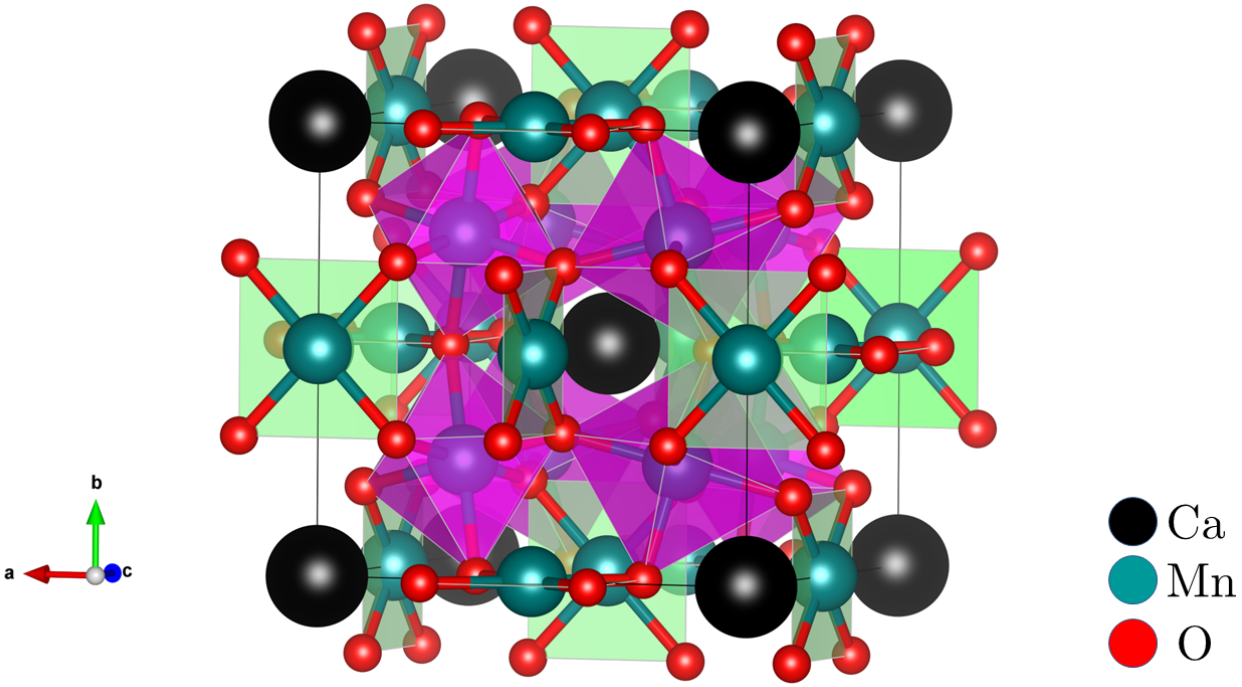

Figure 4.3: Ambient temperature high pressure crystal structure of $CaMn_7O_{12}$. Its lattice is cubic type with spatial group $Im\bar{3}$. Note that in this case, there is only one type of octahedron, depicted in pink.

4.2 Pressure-induced charge-ordering phase transition

In [2], they performed resistivity and single-crystal X-ray diffraction experiments on $CaMn_7O_{12}$ to study its pressure-induced phase transition and to analyze the role of the distortion at the distorted octahedron along the phase transition. The first result relevant for this text is shown in figure 4.4:

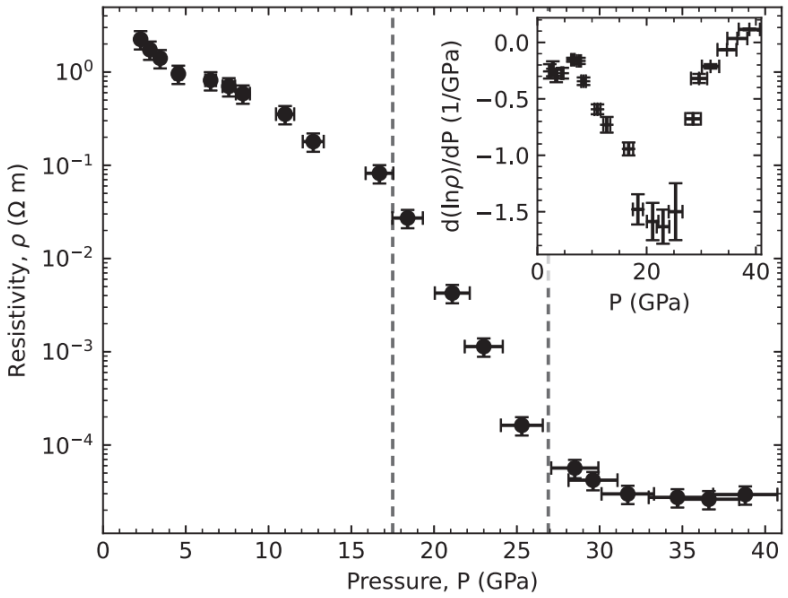

Figure 4.4: Results of resistivity measurements as a function of pressure for $CaMn_7O_{12}$ at ambient temperature. Note the logarithmic scale on the y-axis. The figure has been extracted from [2][Figure 2].

The huge drop in resistivity in the range between 18 and 28 GPa might suggest the existence of a

pressure-induced phase transition, but further investigation is required to verify whether that hypothesis is correct. Figure 4.4 will allow us to check if our DFT calculations are properly predicting the beginning of the pressure-induced phase transition.

The single-crystal X-ray diffraction experiment allowed to obtain the distances in the Mn-O octahedra with pressure (Figure 4.5). In blue, the longest distance in the distorted octahedron. In pink, the distance in the regular octahedron. In yellow, the shortest distance in the distorted octahedron. In green, the points for the high pressure phase, which correspond to the only distance in the regular octahedron in the high pressure phase. All distances converge to a single one at a pressure around 28 GPa. This pressure should be the end of the phase transition according to figure 4.4. The convergence of all distances to a single value is a proof that the two types of octahedra became equivalent positions and hence, the distortion that was affecting the distorted octahedron is gone. It is also remarkable how between 20 and 28 GPa, the shortest distances increase while the largest distance decreases at a higher rate.

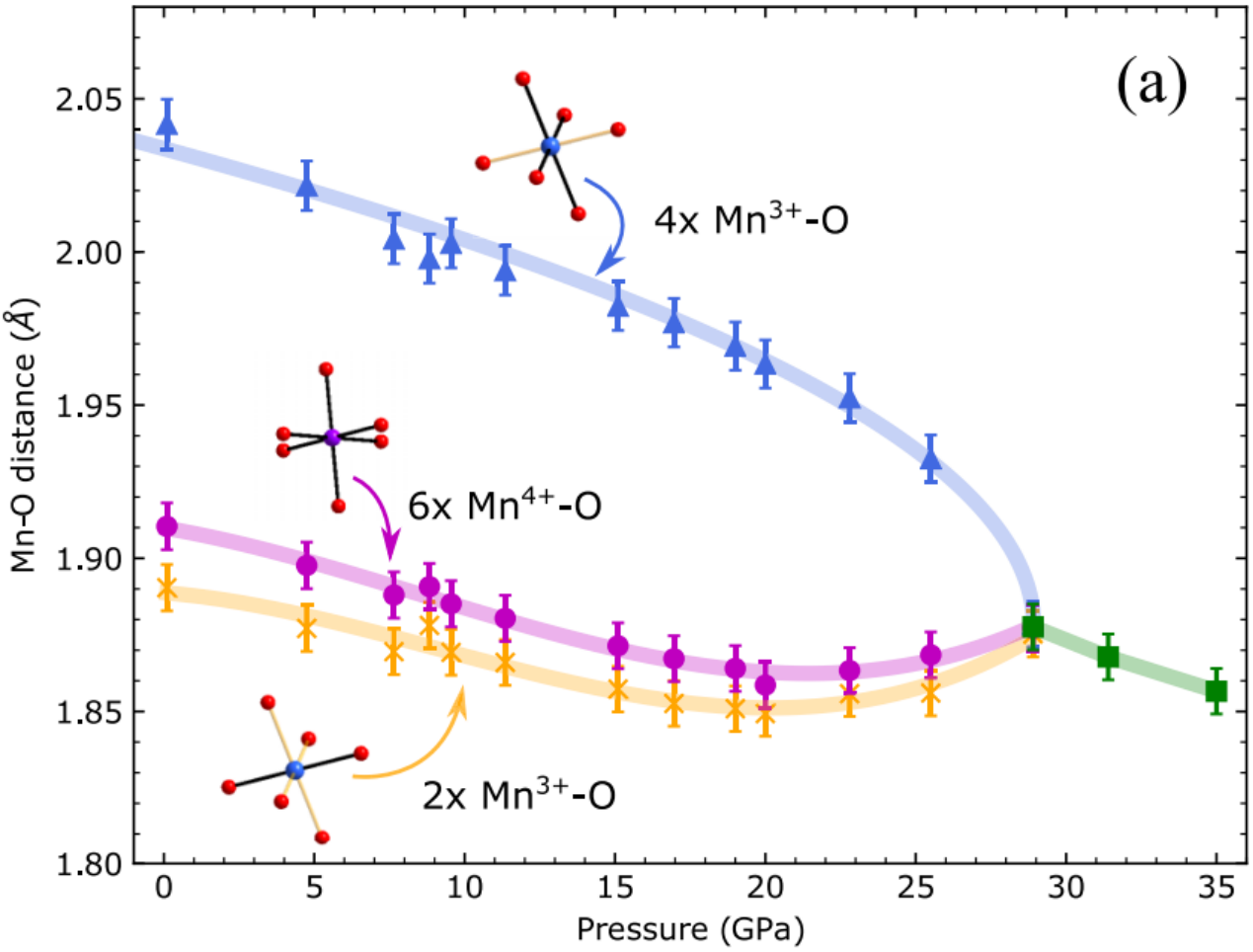

Figure 4.5: Graph of the evolution of the Mn-O distance with pressure. In blue, the longest distance in the distorted octahedron. In pink, the distance in the regular octahedron. In yellow, the shortest distance in the distorted octahedron. In green, the points for the high pressure phase, which correspond to the only distance in the regular octahedron in the high pressure phase. The plain lines are just guides for the eye. The figure has been extracted from [2][Figure 3].

The distortion at the compressed octahedron can be quantified with the Jahn-Teller distortion parameter σ_{JT}. In this text, we will use the definition given in [23][Page 4221]:

$$\sigma_{JT} = \left(\sum_{i=1}^{6} (R_{Mn-O} - \langle R_{Mn-O} \rangle)^2 \right)^{1/2} \tag{4.1}$$

Where R_{Mn-O} is one of the six distances in the octahedron and $\langle R_{Mn-O} \rangle$ is the mean distance. The evolution of this parameter with pressure is shown in figure 4.6. The figure shows how the distortion starts decreasing heavily at around 18 GPa and is completely gone at around 28 GPa. As a consequence, all the octahedra become equivalent, leading to the $R\bar{3}$ to $Im\bar{3}$ phase transition discussed in the previous section. The dashed line shows how the initial tendency would lead to a Jahn-Teller quenching well above 40 GPa. This fact suggests that the Jahn-Teller distortion has not disappeared because of the action of the pressure.

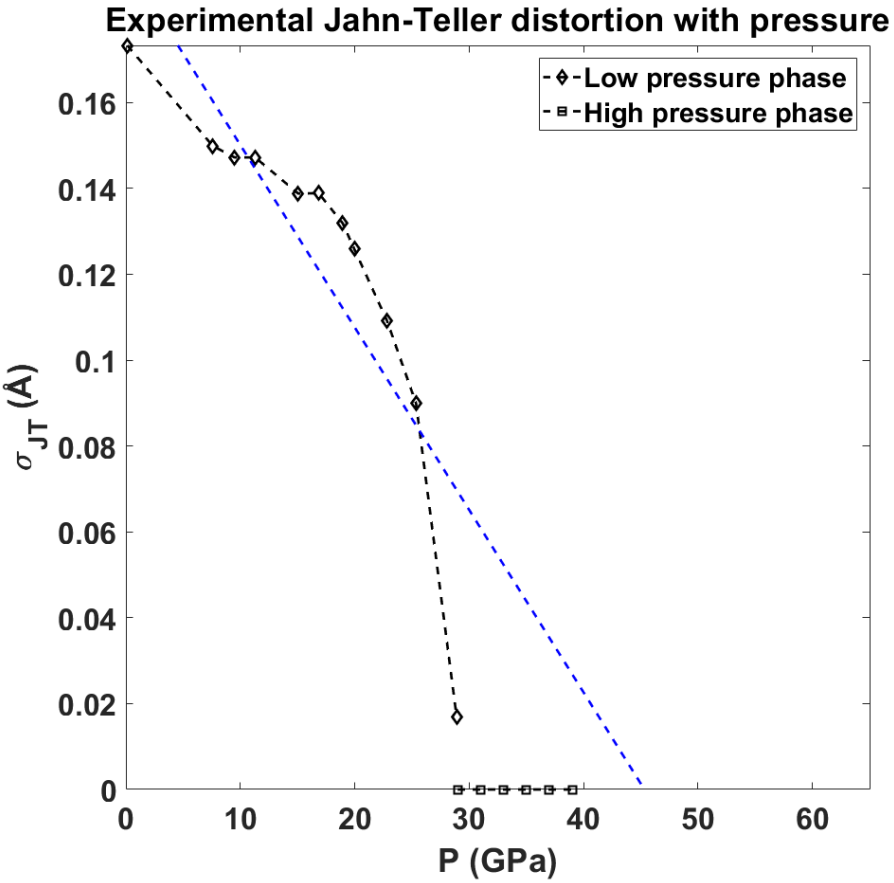

Figure 4.6: Evolution of the distortion affecting the compressed octahedron with pressure. The distortion starts decreasing heavily at around 20 GPa and is completely gone at around 30 GPa. The dashed line shows a linear extrapolation considering the points below 20 GPa. This extrapolation shows the pressure for the Jahn-Teller quenching. Data extracted from [2][Figure 3].

Figure 4.7 shows the evolution of the volume of the different types of Mn-O_6 octahedra. Between 0 and 20 GPa, there is a monotonic decrease in the volumes of the octahedra, consistent with an increase in the hydrostatic pressure. After 20 GPa, we can see how the two different volumes start getting closer one to the other. The volume of the regular octahedra increases between 20 and 28 GPa, getting closer to the volume of the distorted octahedra. At around 28 GPa, the two volumes turn into only one, the phase transition is complete and there is only one type of octahedra

The dashed lines show a fit of the data below 20 GPa to a third order Birch-Murnaghan equation of state [24][Page 5]:

$$P(V) = \frac{3K_0}{2}\left[\left(\frac{V_0}{V}\right)^{\frac{7}{3}} - \left(\frac{V_0}{V}\right)^{\frac{5}{3}}\right]\left\{1 + \frac{3}{4}\left(K_0' - 4\right)\left[\left(\frac{V_0}{V}\right)^{\frac{2}{3}} - 1\right]\right\} \tag{4.2}$$

Where K_0 is the bulk modulus and K_0' is its derivative. Mathematically:

$$B_0 = -V\left(\frac{\partial P}{\partial V}\right)_{P=0} \tag{4.3}$$

$$B_0' = \left(\frac{\partial B}{\partial P}\right)_{P=0} \tag{4.4}$$

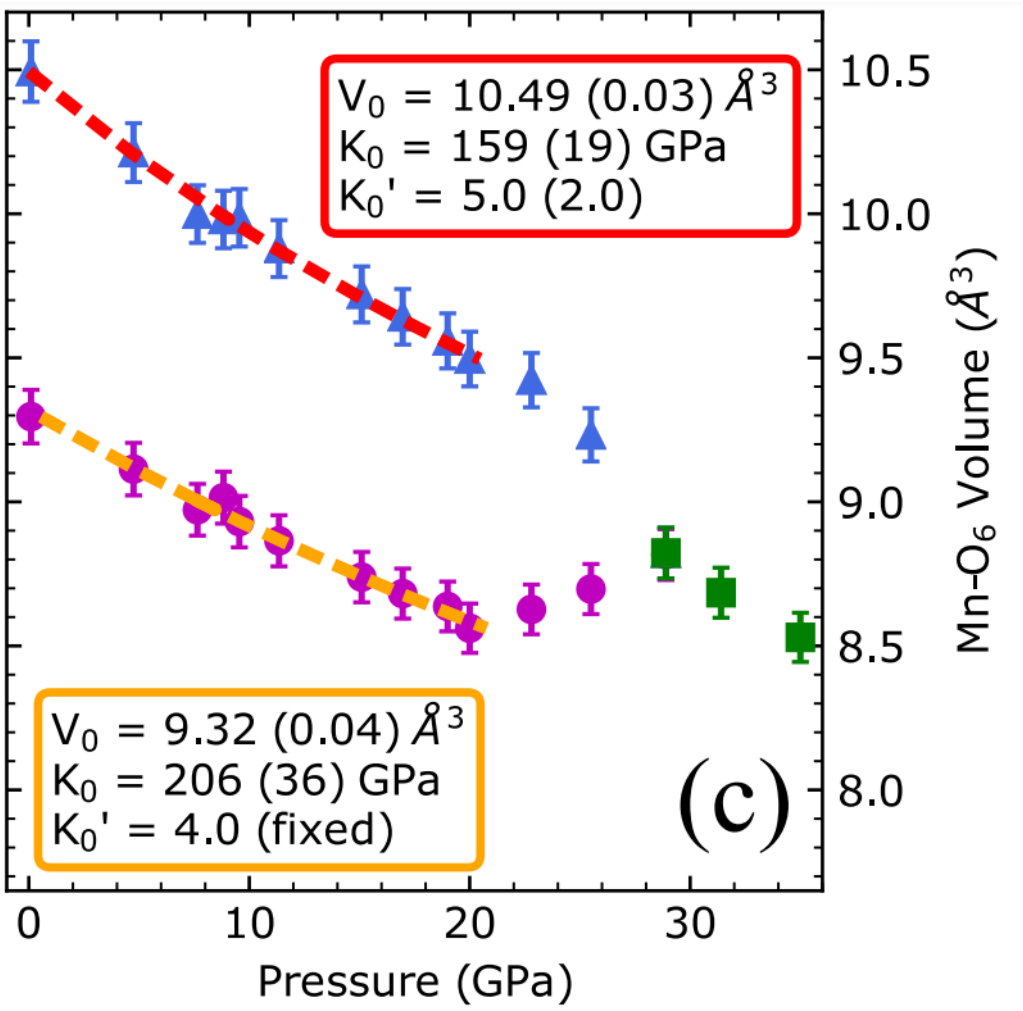

Figure 4.7: Evolution of the volume of the Mn-O_6 octahedra. In blue, points for the distorted octahedra. In pink, points for the regular octahedra. In green, points for the regular octahedra of the high pressure phase. The dashed lines show the fit of the data below 20 GPa to a third order Birch-Murnaghan equation of state [24][Page 5]. The figure has been extracted from [2][Figure 3].

The lattice parameters (Figure 4.8 (a)) are two below 30 GPa. Around 30 GPa, there is a change from having two different parameters to only one. This is consistent with a phase transition between the $R\bar{3}$ phase and the $Im\bar{3}$ phase.

There is a monotonic decrease in the cell volume (Figure 4.8 (b)) as pressure increases. The dashed line is a fit of the data to a third order Birch-Murnaghan equation. Its range is shown by the dashed line itself.

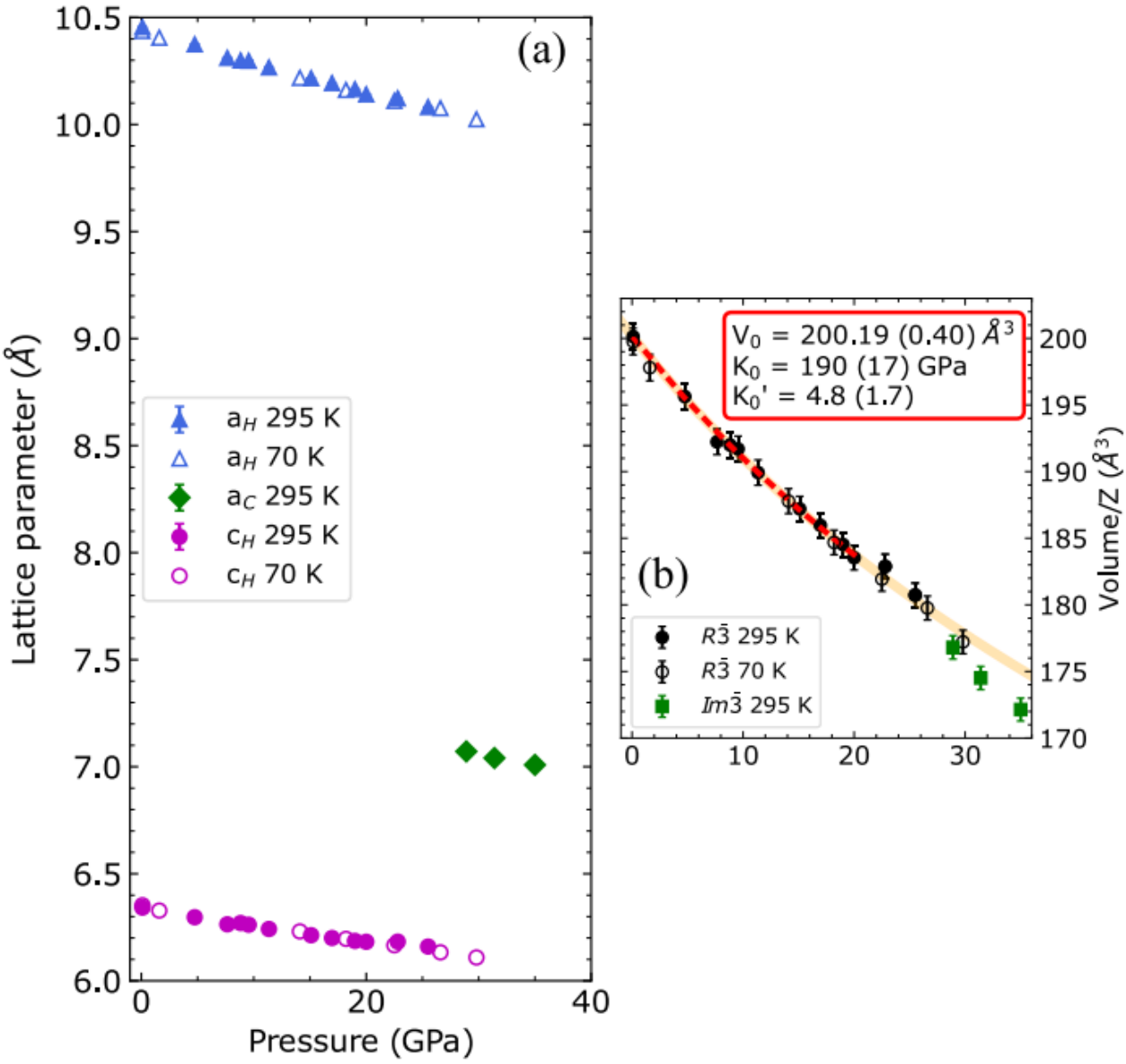

Figure 4.8: (a) Evolution of the lattice parameters a and c with pressure. The subindex $_c$ corresponds to the cubic phase whereas the subindex $_H$ corresponds to the rombohedral phase.
(b) Evolution of the cell volume with pressure. The dashed line is a fit of the data to a third order Birch-Murnaghan equation. Its range is shown by the dashed line itself. The yellow straight line is just a guide for the eye that shows the extrapolation of the fit. The /Z in the y-axis is an erratum.
The figure has been extracted from [2][Figure 4].

In [2], they claim that the mechanism of this phase transition is via charge ordering with the Mn^{3+} changing to a new oxidation state. How can we infer that with the results presented in this text? Let us recall some conclusions of the previous figures:

- Figure 4.4 shows a huge drop in resistivity. As a consequence, we can conclude that there has been some charge delocalization during the phase transition.
- Figure 4.6, specifically, its linear extrapolation, hints that the Jahn-Teller pressure quenching should happen at around 45 GPa. However, the Jahn-Teller distortion is extinct at 28 GPa. This fact suggests that pressure has not been the agent responsible for the vanishing of the Jahn-Teller distortion.

These two deductions already hint the charge-ordering mechanism, but the pressure quenching of

the Jahn-Teller distortion must still be discarded.

To do so, the ideas of [25] can be used. In that paper, it is shown how the Jahn-Teller quenching pressure can be estimated with the Jahn-Teller energy, E_{JT}, defined as the energy required to turn a D_{4h} distorted octahedron into a O_h regular octahedron. The greater the value of E_{JT}. the bigger the quenching pressure. Under the assumptions[1] of [25], the Jahn-Teller energy can be calculated with the following formula:

$$E_{\mathrm{JT}} = \frac{K_0 V_0}{K_0'} \left(\frac{x^{1-K_0'} - K_0'}{K_0' - 1} + x \right) \tag{4.5}$$

Where $x = {}^{V_{crit}}/_{V_0}$ and V_{crit} is the final volume of the regular octahedron (Right after the phase transition is complete). V_0, K_0 and K_0' are the fit parameters of the third order Birch-Murnaghan equation as shown in equation (4.2).

With this method, they obtain for Mn-O_6 distorted octahedron in $LaMnO_3$ that $E_{\mathrm{JT}} = 0.25$ eV with $P_{crit} \approx 30$ GPa [25][Page 4]. In [2][Page 5], they obtain for the distorted octahedron in $CaMn_7O_{12}$ that $E_{\mathrm{JT}} = 0.46$ eV, which is higher than that for the same type of octahedron in $LaMnO_3$ and as a result, P_{crit} must be greater than 30 GPa in the case of $CaMn_7O_{12}$.

However, the Jahn-Teller distortion is already gone by 30 GPa. It is concluded then that pressure is not responsible for the quenching of the Jahn-Teller distortion and that another mechanism must be behind it.

In [19], a temperature-induced charge-ordering phase transition is reported. In this phase transition, the Mn^{3+} changes to a $Mn^{3.25+}$ oxidation state.

After this discussion and in analogy with the temperature-induced charge-ordering phase transition reported in [19] it is concluded that the mechanism of the phase transition must be a change in the charge ordering with the Mn^{3+} changing to $Mn^{3.25+}$.

[1] Which are quasiadiabatic conditions and a Murnaghan equation of state: $P(V) = \frac{K_0}{K_0'} \left[\left(\frac{V}{V_0} \right)^{-K_0'} - 1 \right]$.

Chapter 5

Results and analysis

5.1 Finding the proper parameters for convergence

After following the procedure of section 3.5, the results shown in figures 5.1 and 5.2 were obtained.

Figure 5.1 shows the energy cutoff convergence (left) and the k-points convergence (right) for the low pressure phase. The energy difference has already converged for energy cut offs of 300 eV and above. For the k-points convergence, note that the scale is of the order of 10^{-3}. The converged values on Figure 5.1 left are about this exact same order of magnitude. This means that all values in figure 5.1 can be considered converged (with the chosen energy cutoff) .

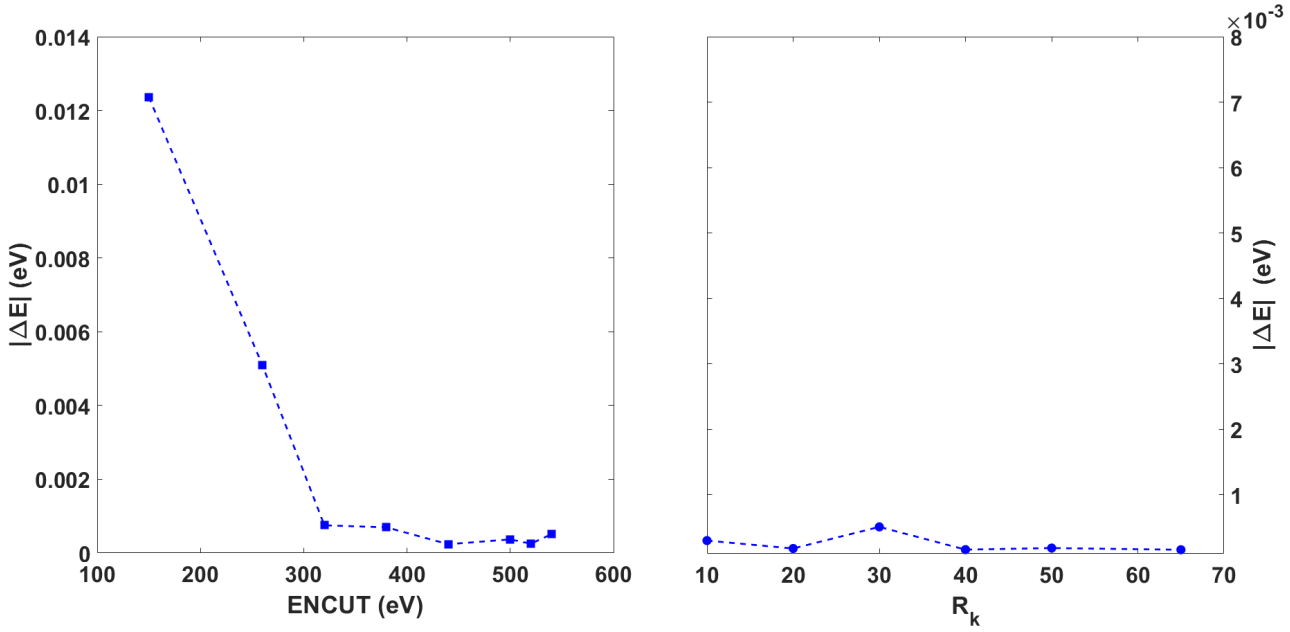

Figure 5.1: Convergence results for the low pressure phase. The difference in energy $|\Delta E|$ is taken as the internal energy of the system with a 194.755 Å^3 volume cell minus the internal energy of the system with a 194.72 Å^3 volume cell. On the left, the behaviour of $|\Delta E|$ as a function of the energy cutoff with a $6 \times 6 \times 6$ mesh. On the right, the evolution of $|\Delta E|$ with the parameter R_k, which controls the number of k-points in the mesh with an energy cutoff of 540 eV.

Figure 5.2 shows the energy cutoff convergence (left) and the k-point (right) convergence for the high pressure phase. The energy difference has already converged for energy cutoffs of about 450 eV and above. The case of convergence as a function of R_k is more clear this time. All points have a $|\Delta E|$ of the order of 10^{-3} , which is good enough. For values of R_k of 45 and above, the energy difference seems to converge to a value of 10^{-3}.

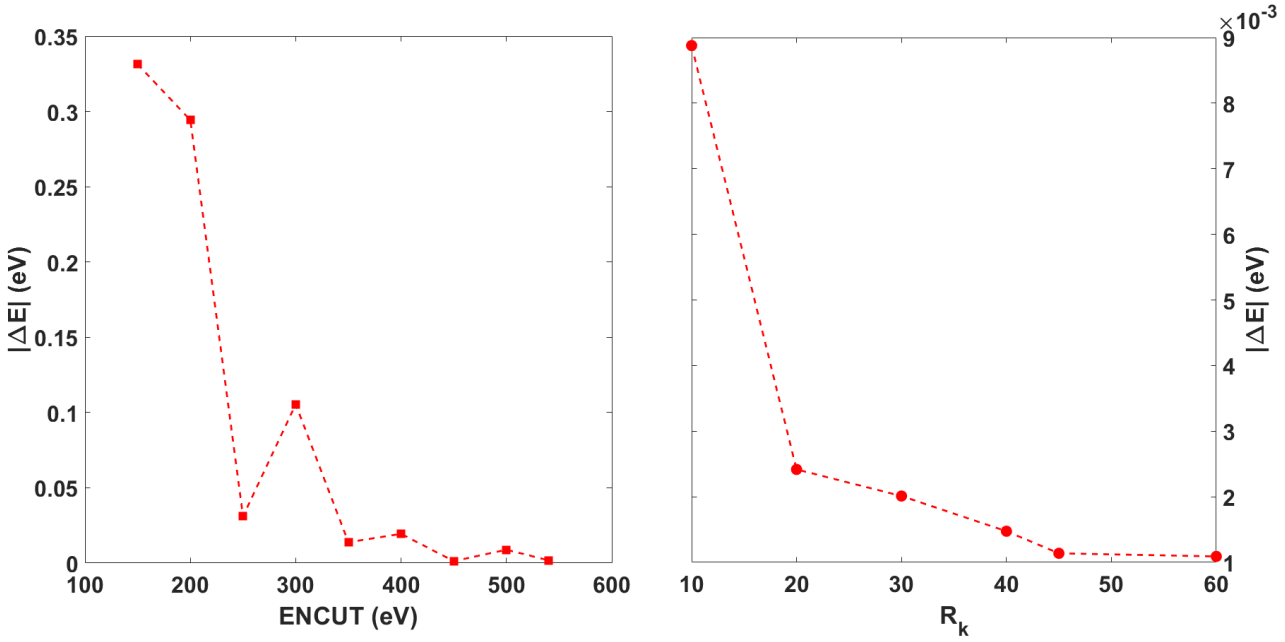

Figure 5.2: Convergence results for the high pressure phase. The difference in energy $|\Delta E|$ is taken as the internal energy of the system with a 191.05 Å^3 volume cell minus the internal energy of the system with a 191.6 Å^3 volume cell. On the left, the behaviour of $|\Delta E|$ as a function of the energy cutoff with a $6 \times 6 \times 6$ mesh. On the right, the evolution of $|\Delta E|$ with the parameter R_k, which controls the number of k-points in the mesh with an energy cutoff of 540 eV.

From the analysis of the two previous cases, we find out that:

- For both phases (high and low pressure), the energy difference has converged for energy cutoffs above 450 eV.
- For both phases (high and low pressure), the energy difference is low enough for values of R_k above 40.

The rest of the calculations were carried out with an energy cut off of 500 eV and a $R_k = 40$. $R_k = 40$ corresponds to an $8 \times 8 \times 8$ mesh.

5.2 Band structure and gap as a function of the Hubbard parameter

Table 5.1 shows the value of the band gap for different values of the U *Hubbard parameter*. We can observe an increase in the energy band gap as U increases. This tendency is also reported in [26][Figure 7] and [27][Figure 3]. The energy band gap was found to be indirect in every case and always between the same k points of the path followed.

U (Hubbard parameter)	5	4	3.5	3	2
Energy band gap (eV)	0.7435	0.4221	0.2369	0.0472	0

Table 5.1: Values of the energy band gap as a function of the U *Hubbard parameter*.

The influence of the U *Hubbard parameter* on the band structure can be noted in figure 5.3. For U=2, $CaMn_7O_{12}$ is a metal, with no gap at all. Several bands cross the Fermi level. For the rest of the values of U, $CaMn_7O_{12}$ behaves as a semiconductor, with a very small band gap. Despite the increase in the band gap with increasing U, the shape of the bands remains almost unchanged. The indirect band gap is specified for the case U=3.5 with a double arrow. When explaining DFT+U functionals, we

stated that DFT+U served as a better description of d and f electrons than DFT by itself. The particular influence on d bands can be observed in figure 5.4. This figure shows the spin-dependent total density of states with the contributions of the p oxygen electrons and the d manganese electrons. All DOSs are affected by the change in U. Regarding the $3d$ bands, their location in energy changes with U but not their energy bandwidth.

The energy band gap can also be observed with the DOS. Figure 5.5 is a closer look at the DOS around the band gap (using the same energy range as in the band structure of figure 5.3). For U=3, the band gap is so small that the energy resolution available is not enough to see the actual band gap. With this zoom-in, We can see that the band gap corresponds to transitions from the $2p$ oxygen orbitals to $3d$ manganese orbitals. This transition is dipole allowed and hence, optically accessible.

In [19][Page 4], they claim the electronic band gap of $CaMn_7O_{12}$ is 240 meV. For U$=$ 3.5, we obtained a bandgap of 236.9 meV which is consistent with the cited result. Therefore, we chose U=3.5 as the appropiate value for the description of the electronic properties and the structure. In the following sections, only the results for U=3.5 will be presented. The results for the rest of the U *Hubbard parameters* are left for chapter 6.

But why a good description of the electronic properties should translate into a good description of the structure? The structure is determined by all electrostatic interactions. The most important ones are those of the outer shell electrons, which interact with the electrons of other ligands and participate in the bonding. If we manage to find a good description of all the electrons and in particular, of those of the outer shells that interact with electrons of other atoms, we will have found a good description of the electrostatic interactions between atoms and since these determine the structure, we will have found a good description of the structure. The following sections will serve as the acid test for this reasoning.

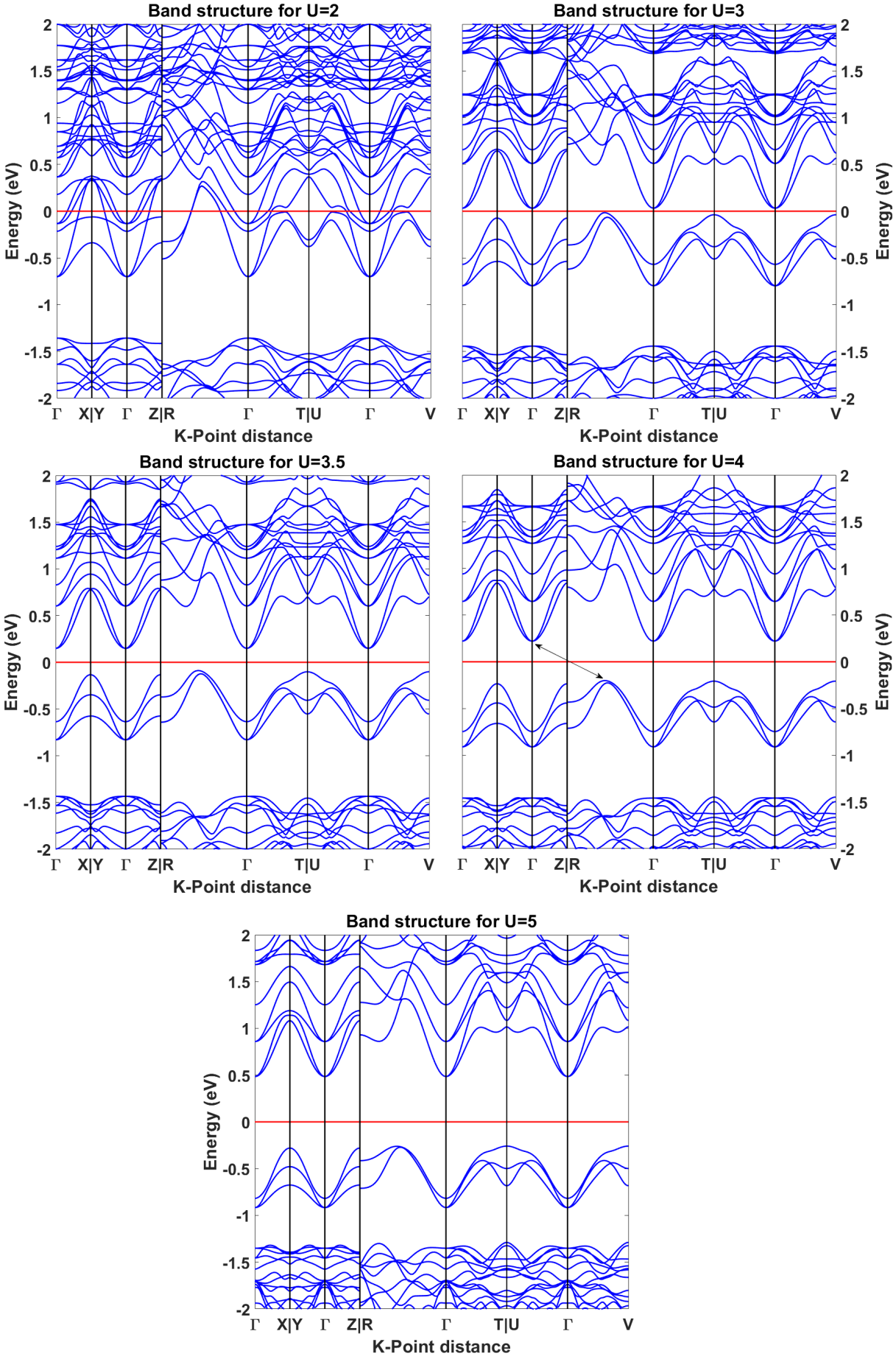

Figure 5.3: Band structure for each value of the U *Hubbard parameter* along the high symmetry path $\Gamma - X|Y - \Gamma - Z|R - \Gamma - T|U - \Gamma - V$. The red line (zero energy) is located at the chemical potential.The x-axis indicates the high symmetry path along the first Brillouin zone. The double arrow on the U=3.5 plot shows the indirect gap.

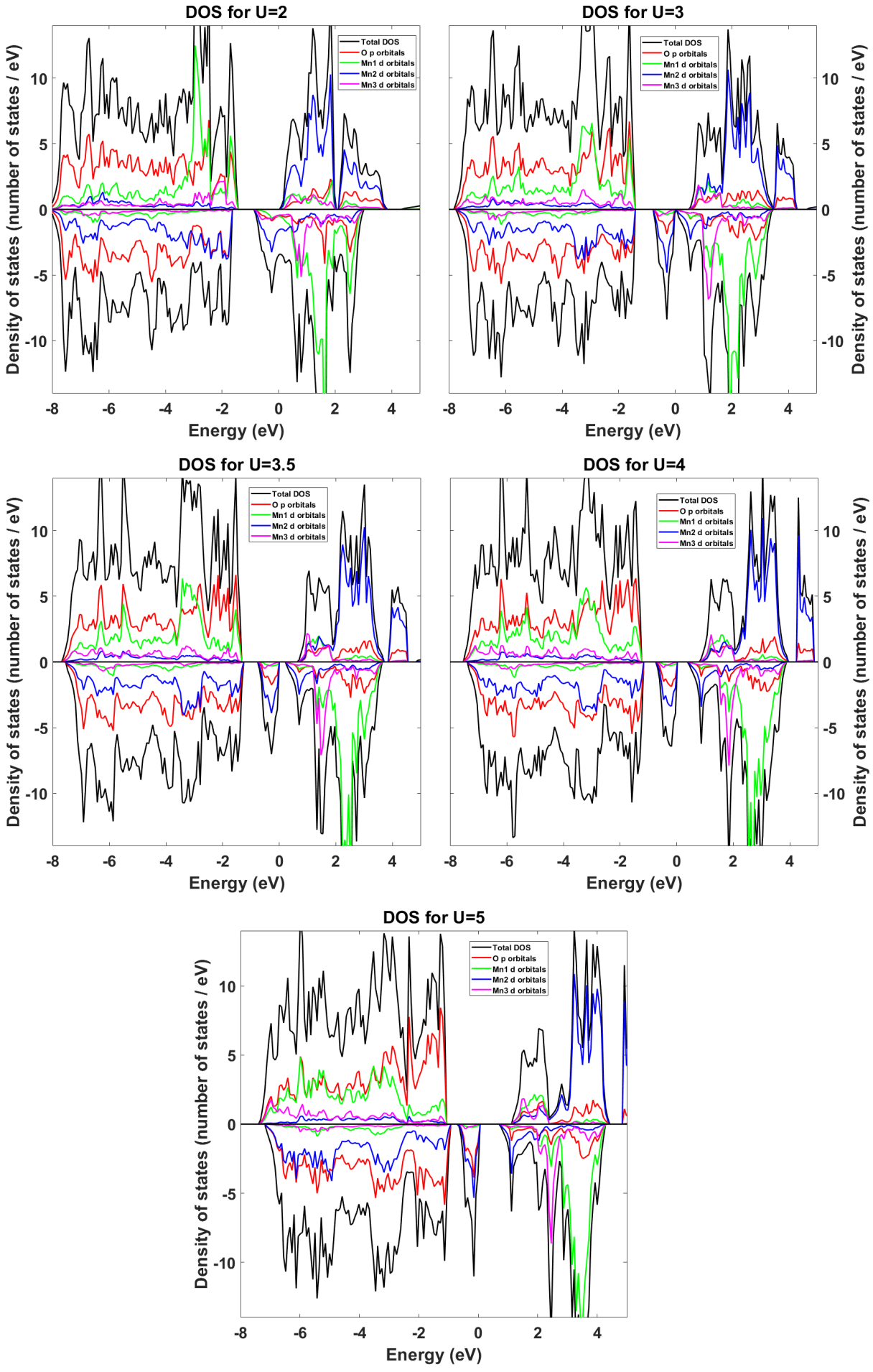

Figure 5.4: Density of states for different orbitals and values of the U *Hubbard parameter*. Positive density is spin up DOS whereas negative density is spin down DOS. Zero energy corresponds to the value of the chemical potential. The energy range was chosen to observe the influence of U on the distribution in energy of the orbitals.

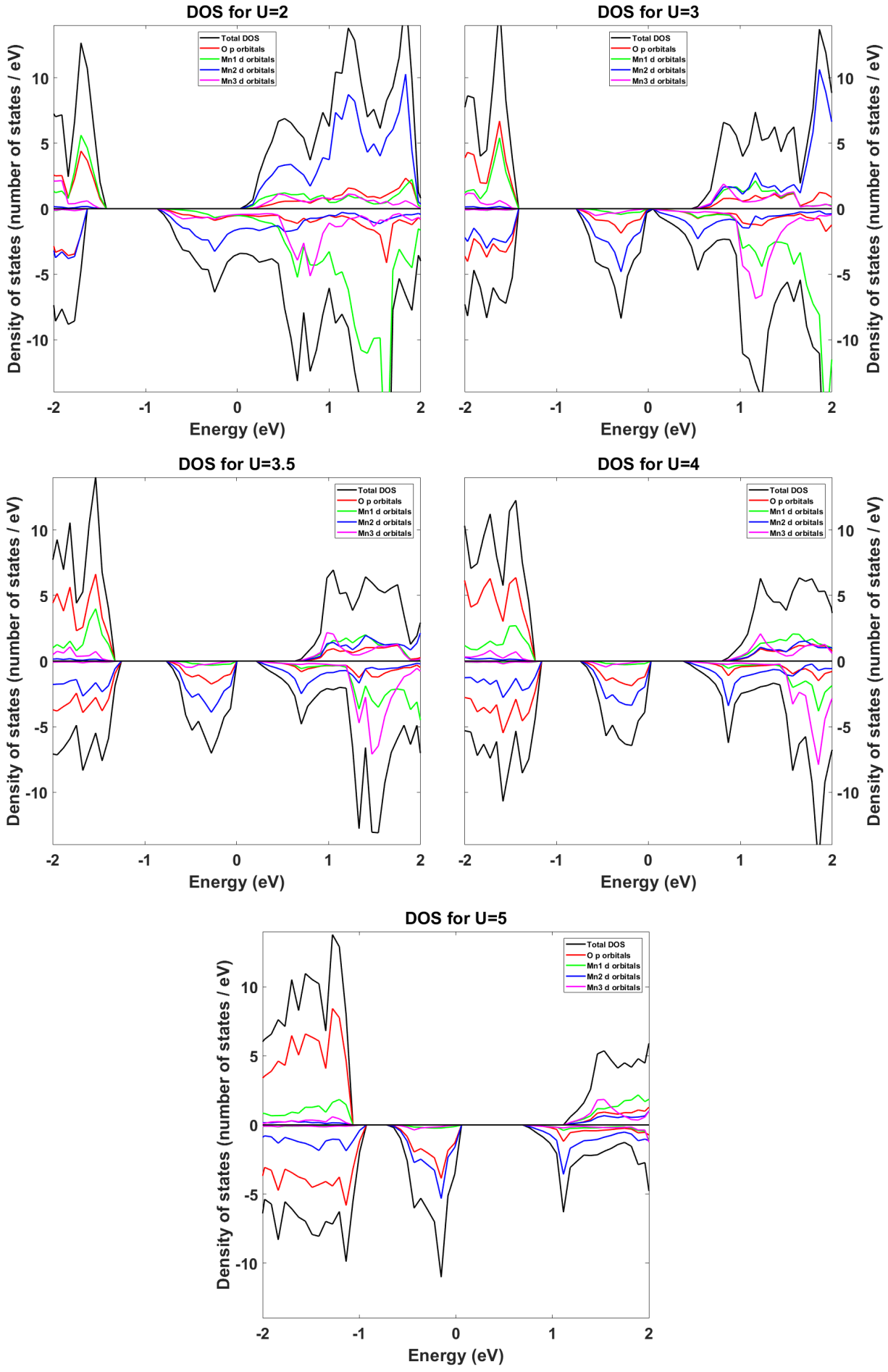

Figure 5.5: Density of states for different orbitals and values of the U *Hubbard parameter* around the band gap. Zero energy corresponds to the value of the chemical potential.

5.3 Stability of each phase and the phase transition: enthalpy

The stability of a phase can be measured via thermodynamic potentials. Every thermodynamic potential (excluding entropy) decreases when transiting to a more stable phase. In our case, we can use enthalpy as the thermodynamic potential to check the stability of the high pressure phase vs the low pressure phase. Enthalpy H is defined as:

$$H = U + PV \tag{5.1}$$

Where U is the internal energy of the system, P its pressure and V its volume. The difference in enthalpy between the high pressure phase and the low pressure phase (Figure 5.6) changes its sign at around 20 GPa indicating the beginning of the phase transition. Hence, the $Im\bar{3}$ phases starts being more stable from 20 GPa. This is consistent with the resitivity measurements (Figure 4.4) that concluded the phase transition takes place between 18 and 28 GPa, having a phase coexistence due to the first order nature of the phase transition.

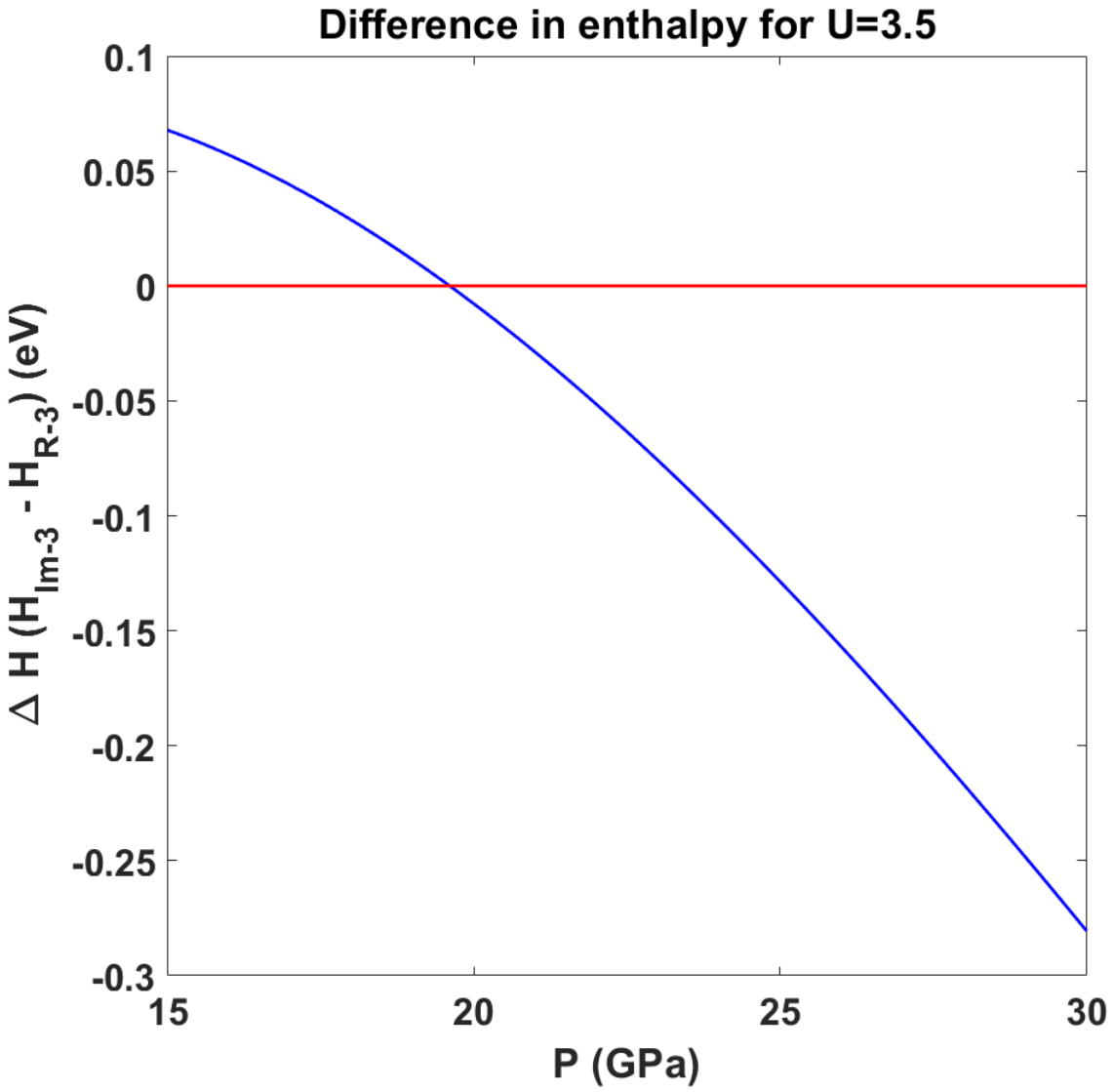

Figure 5.6: Difference in enthalpy between the high pressure phase ($Im\bar{3}$ phase) and the low pressure phase ($R\bar{3}$) phase. The red line marks the zero value. The difference turns negative at around 20 GPa, indicating that the phase transitions starts at that value.

5.4 Long-range order structure

According to the agreement of the electronic structure with experimental information for U=3.5, we should observe good agreement as well for the structure-related magnitudes.

The pressure evolution of cell volume (Figure 5.7 left) is very similar to the experimental data (Figure 4.8 (b)), with a starting point around 200 Å^3, a complete phase transition around 28 GPa and the volume of the high pressure phase well around 175 Å^3. We can check the similarity between computational and experimental data with the fits to a third order Birch-Murnaghan equation of state. Considering the errors shown in figure 4.8 (b), the values for K_0 and K_0' obtained here are compatible. The opposite goes for V_0 which does not overlap with the error interval. Nevertheless, the value presented here is very close to the one in figure 4.8 (a).

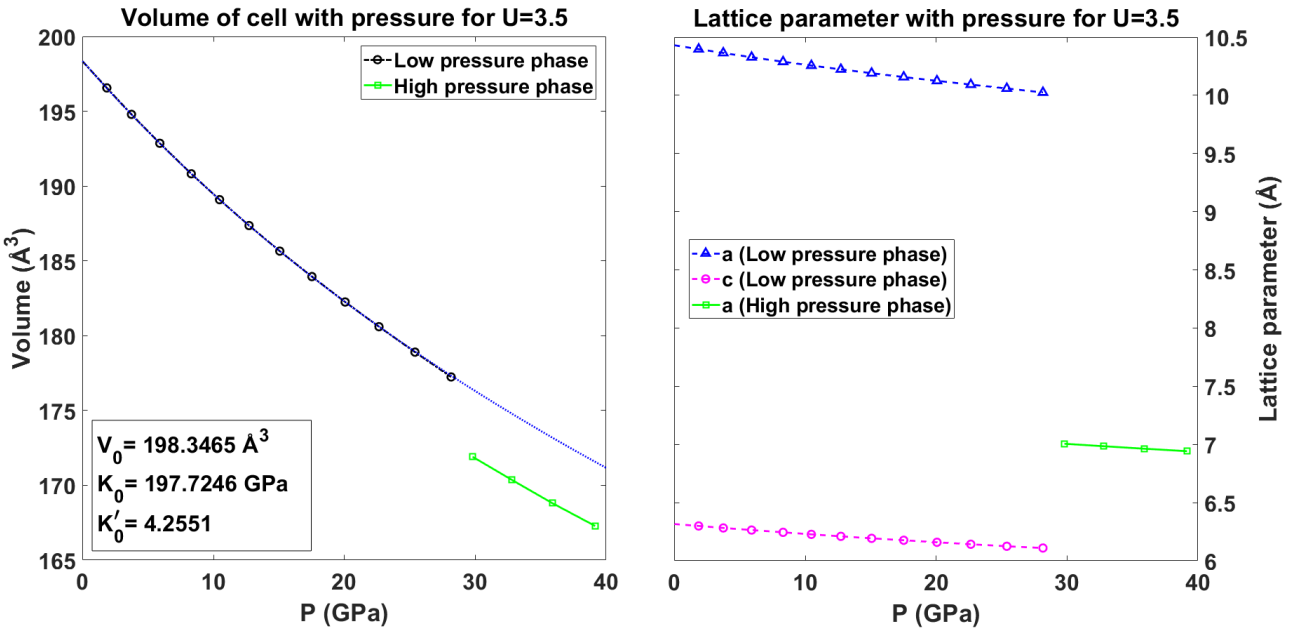

Figure 5.7: (Left) Volume of the primitive cell under pressure. The dashed line is a fit to a third order Birch-Murnaghan equation of state with parameters shown in the bottom-left side of the plot. The points considered for the fit are those under 20 GPa.
(Right) Value of the lattice parameters under pressure. The rhombohedral low pressure phase has two lattice parameters whereas the cubic high pressure phase has one.

The lattice parameters (Figure 5.7 right) present a great agreement with the experimental ones (Figure 4.8). For the lattice parameter a of the low pressure phase, we observe its starting point around 10.5 Å, reaching a value around 10 Å right before the phase transition is complete, which compares very well with figure 4.8 (a). The values of c lie between 6.5 and 6 Å approximately, in good agreement with the experimental data of figure 4.8 (a). The few values for the high pressure phase are around 7 Å both computationally and experimentally.

5.5 Short-range order structure

The Jahn-Teller distortion with pressure (Figure 5.8 left) features a linear decrease in the distortion with pressure that can be observed up to 28-30 GPa. The linear tendency is already broken between the last two points of the low pressure phase, where a greater decrease can be observed. After 28-30 GPa, the high pressure phase is present, and hence, the distortion is vanished. This vanishing of the distortion coincides with the ending of the phase transition. The linear extrapolation made with the points of the low pressure phase indicates that the Jahn-Teller quenching pressure should be around 59 GPa, suggesting that the vanishing of the distortion has not been produced by pressure itself but

by other factors.

The values of the distortion presented here are of the same order of magnitude that of experimental ones (Figure 4.6). At around 0 GPa, the value of σ_{JT} is around 0.17 Å both in experiment and calculations. Then , it drops to 0.08 Å right before the ending of the phase transition.

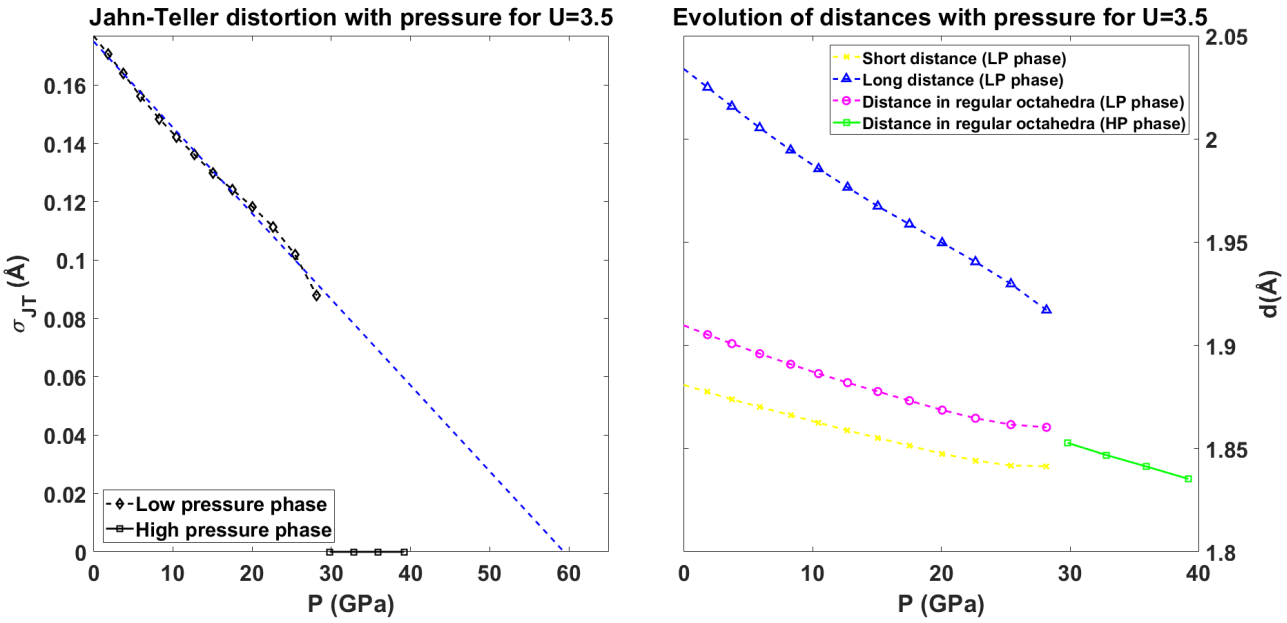

Figure 5.8: (Left) Evolution of the Jahn-Teller distortion with pressure. The dashed line shows a linear extrapolation. The fit is done to the points of the low pressure phase.
(Right) Evolution of the distances in the different types of Mn-O_6 octahedra.

Figure 5.8 right shows the evolution of the distances in the different octahedra with pressure. All distances decrease monotonically with pressure and converge to one after around 28 GPa i.e after the phase transition. After the phase transition (Above 28 GPa) there must be only one distance since the present phase is the cubic high pressure phase.

Comparing with the experimental values of figure 4.5, we can see both qualitative and quantitative agreement for all the different distances. It is remarkable how the GGA+U calculations also reproduce the change in the slope of the pink and yellow curves (corresponding to the distance in the regular octahedra and the short distance in the distorted octahedra respectively). The experimental data of figure 4.5 shows a smoother slope in the range of 15-30 GPa with an slight increase for these curves. The same feature can be seen in figure 5.8 right.

Figure 5.9 represents the behaviour of the volume of the different types of octahedra with pressure. For all the octahedra, the volume decreases under pressure. Again, after around 28 GPa the phase transition is over and hence, we have only one type of octahedra.

Comparing with figure 4.7, the agreement between the experimental data and the computational results is good both qualitatively and quantitatively. In fact, figure 5.9 shows a change in the slope of volume of the regular octahedra between 25 and 30 GPa, almost changing to an increasing tendency (as in figure 4.7). A good way to compare the results is by comparing the fit parameters of the third order Birch-Murnaghan equations. Starting with the distorted octahedra (data in blue), we can see that the values of K_0 and K_0' are compatible considering the error with those of the fit to the experimental data. The case for V_0 is different since the value obtained here does not lie in the error interval of the value of figure 4.7. However, the absolute difference is very small. Following with the regular octahedra (data in pink), the value we obtain for V_0 is compatible with the one in figure 4.7.

For K_0 and K_0', it is the other way around. However, we must take into consideration that the fit of 4.7 fixes K_0' to be 4 whereas the one in figure 5.9 lets K_0' free.

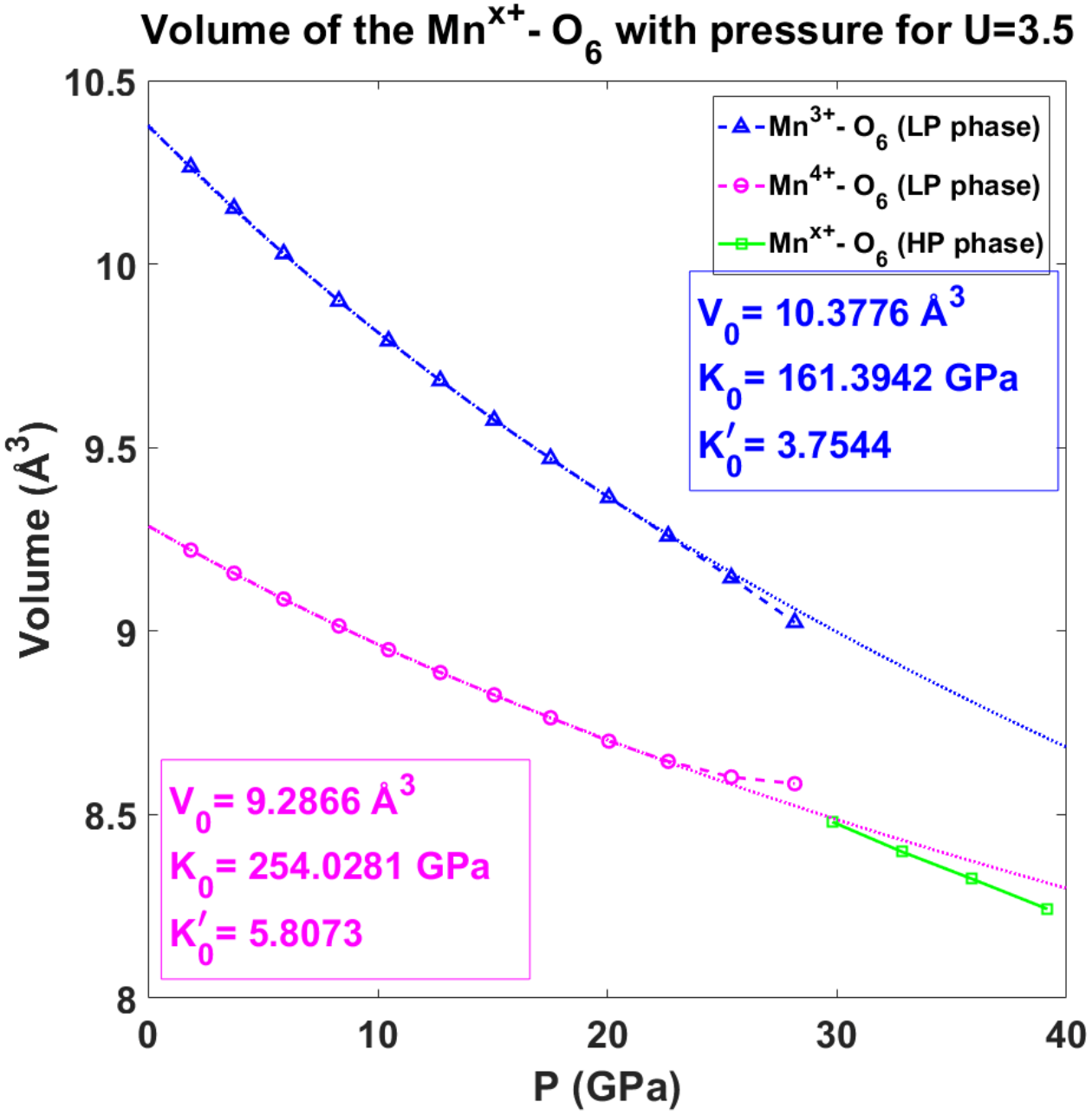

Figure 5.9: Evolution of the volume of the different types of octahedra with pressure. For the octahedra of the low pressure phase, there are fits to a third order Birch-Murnaghan equation considering those points below 20 GPa. The fit parameters are shown in the figure. The octahedra of the high pressure phase are labeled as Mn^{x+}- O_6 due to the fact that the charge-ordering phase transition changes the charge of the Mn at the octahedra.

After having analyzed the structural properties of $CaMn_7O_{12}$ for U=3.5, we have seen a very good agreement with experimental data for all magnitudes considered. Therefore, we have verified that our good electronic description of the system leads to a good description of the structural properties.

Chapter 6

Results for the rest of the *Hubbard parameters*

In the previous chapter we checked how according to the electronic properties, the U *Hubbard parameter* for the best description of the structural properties of $CaMn_7O_{12}$ was U=3.5. In this chapter, we can double check it by taking a look the results for the rest of the U values considered. Some features are similar to the ones seen for U=3.5, hence, we will only comment the relevant features worth mentioning.

6.1 The case U=3

6.1.1 Enthalpy difference

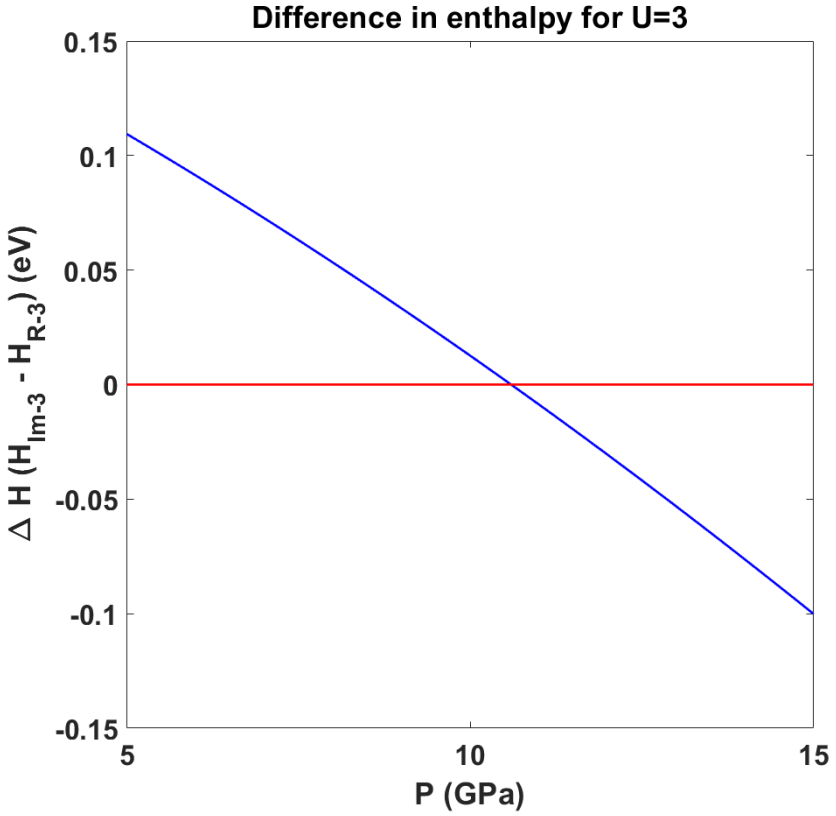

Figure 6.1: Difference in enthalpy between the high pressure phase ($Im\bar{3}$ phase) and the low pressure phase ($R\bar{3}$) phase. The red line marks the zero value. The difference turns negative at around 10 GPa, indicating that the phase transitions starts at that value.

Figure 6.1 represents the difference in enthalpy between both phases. The change of sign of ΔH lies between 10 and 11 GPa. However, experimental results, in particular figure 4.4, show that the beginning of the phase transition lies somewhere between 18 and 28 GPa, a range of pressures incompatible with what figure 6.1 offers.

The value U=3 could not describe correctly the electronic structure and neither it does for the beginning of the phase transition.

6.1.2 Long-range order structure

Results for the long-range structure (figure 6.2) are completely different to those for U=3.5 since the phase transition starts way before. The cell volume (Figure 6.2 left) presents a discontinuity around the phase transition about 12 GPa. Similarly, the lattice parameters (Figure 6.2 right) change from two to a single one around 12 GPa.

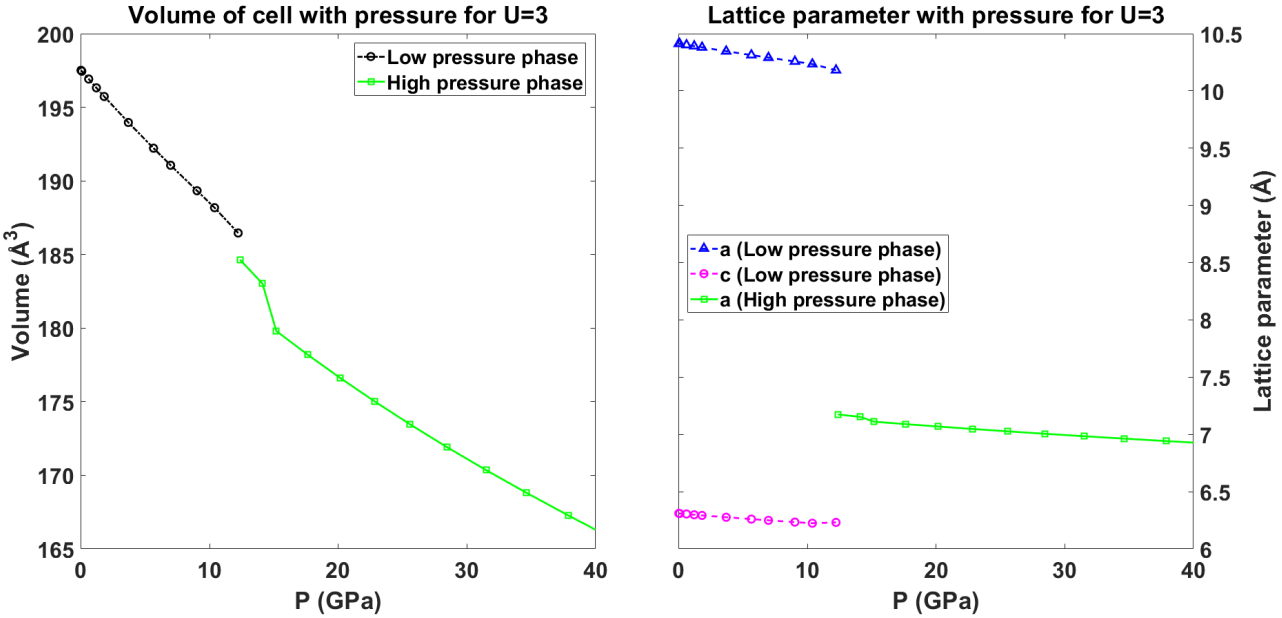

Figure 6.2: (Left) Volume of the primitive cell with pressure.
(Right) Value of the lattice parameters with pressure. The rhombohedral low pressure phase has two lattice parameters whereas the cubic high pressure phase has one.

6.1.3 Short-range order structure

The Jahn-Teller distortion under pressure (Figure 6.3 left) shows a consistent result with figure 6.1. The difference in enthalpy marked the beginning of the phase transition between 10 and 11 GPa and the Jahn-Teller distortion vanishes on that range. Despite being shown as a low pressure phase point, all distances (Figure 6.3 right) converge to a single one around 12 GPa, anticipating the ending of the phase transition.

Figure 6.4 shows the same phenomena through the volume of the Mn-O_6 octahedra. Up to 11 GPa, the volumes of the two different types of octahedra are different, but after 11 GPa, both converge to a single value, indicating that both types become equivalent (and this condition means that there is a phase transition to the $Im\bar{3}$ phase).

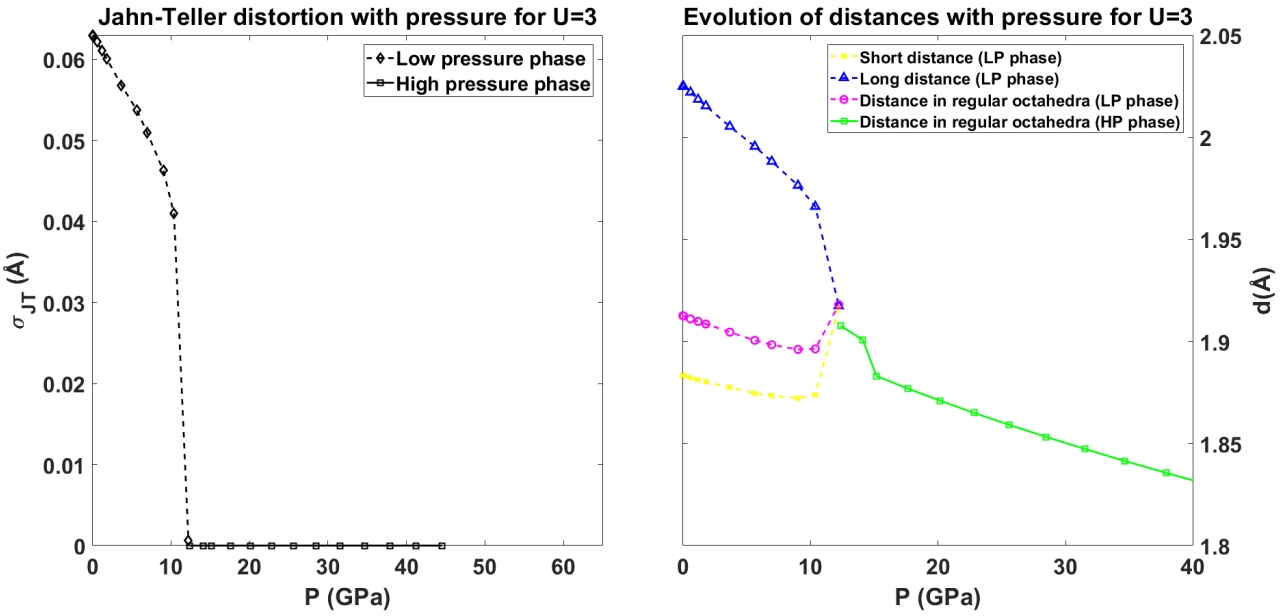

Figure 6.3: (Left) Evolution of the Jahn-Teller distortion with pressure.
(Right) Evolution of the distances in the different types of Mn-O_6 octahedra.

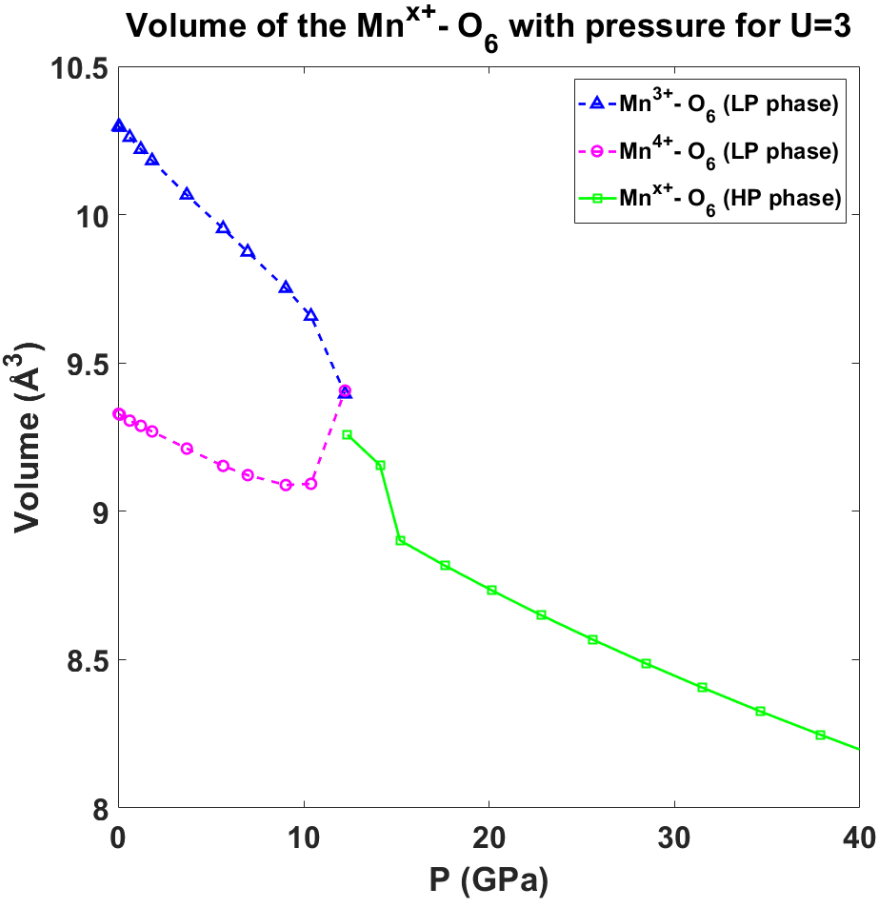

Figure 6.4: Evolution of the volume of the different types of octahedra with pressure. The octahedra of the high pressure phase are labeled as Mn^{x+}- O_6 due to the fact that the charge-ordering phase transition changes the charge of the Mn at the octahedra.

6.2 The case U=4

6.2.1 Difference in enthalpy

The difference in enthalpy for this case is shown in figure 6.5. In this case, the change of sign is about 27 GPa. According to the experimental data exposed in chapter 4, this value is close to the end of the phase transition. Hence, U=4 does not describe well the beginning of the phase transition.

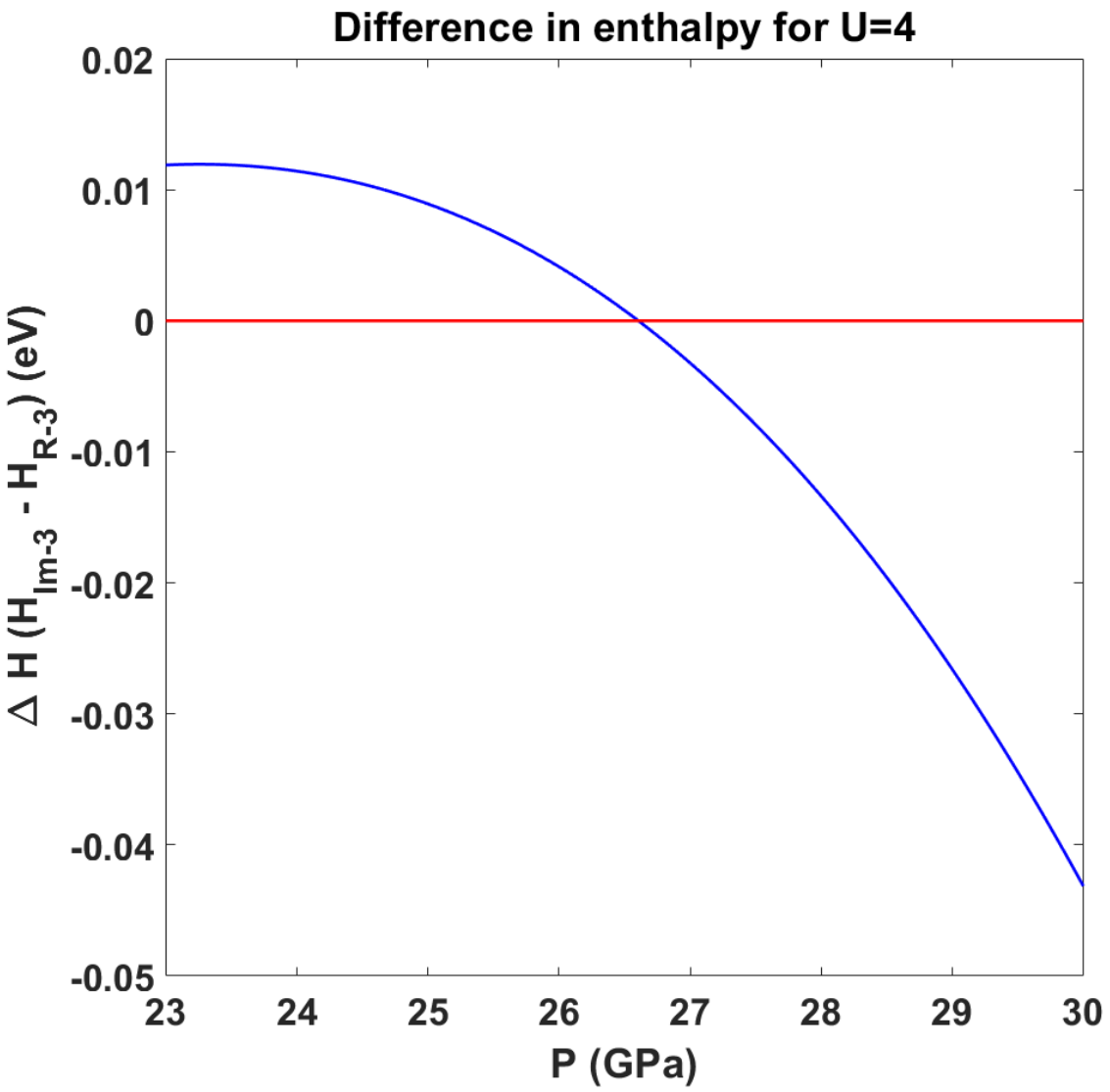

Figure 6.5: Difference in enthalpy between the high pressure phase ($Im\bar{3}$ phase) and the low pressure phase ($R\bar{3}$) phase. The red line marks the zero value. The difference turns negative at around 27 GPa, indicating that the phase transitions starts at that value.

6.2.2 Long-range order structure

The long-range structure for U=4 does not yield anything relevant in comparison with U=3.5. The evolution of the volume of the primitive cell (Figure 6.6 left) is extremely similar to the one for U=3.5. Even the fit parameters to the third-order Birch-Murnaghan equation are almost equal. The behaviour of the lattice parameters with pressure is also extremely similar to the case for U=3.5. These two magnitudes do not show anything relevant.

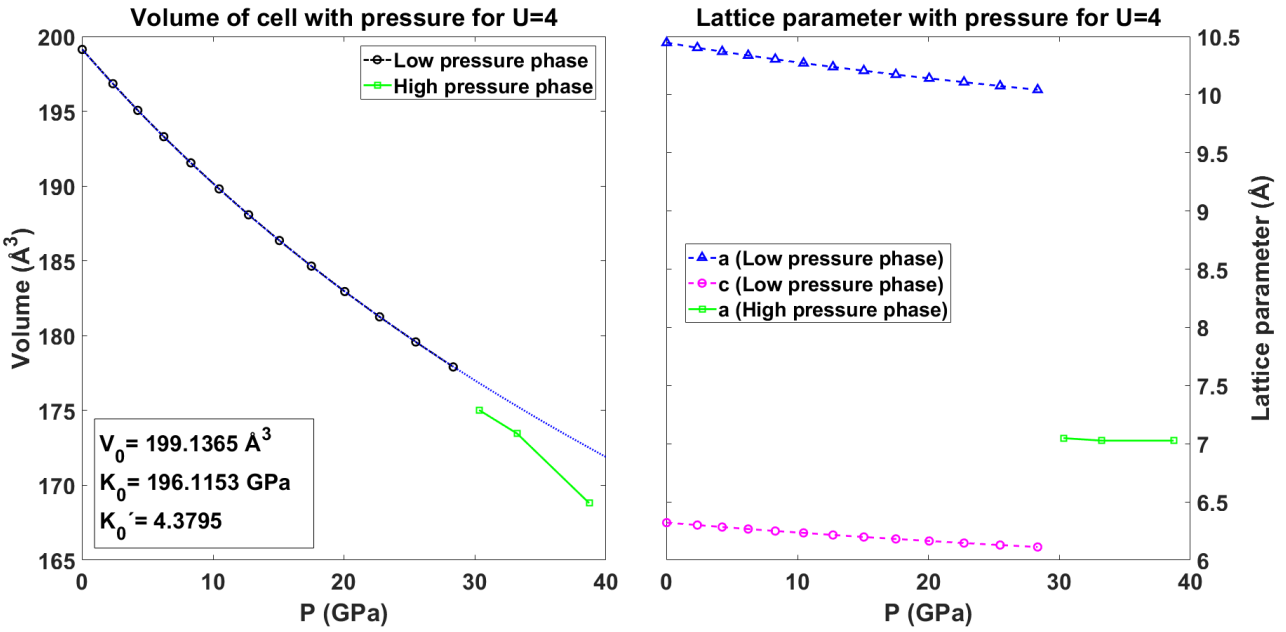

Figure 6.6: (Left) Volume of the primitive cell with pressure. The dashed line is a fit to a third order Birch-Murnaghan equation of state with parameters shown in the bottom-left side of the plot. The points considered for the fit are those under 20 GPa.
(Right) Value of the lattice parameters with pressure. The rhombohedral low pressure phase has two lattice parameters whereas the cubic high pressure phase has one.

6.2.3 Short-range order structure

The Jahn-Teller distortion (Figure 6.7 left) starts from 0.18 Å at 0 GPa (0.17 Å experimentally) and gets to 0.12 Å right before the phase transition (0.09 Å experimentally). Despite the general decreasing trend is consistent with experimental data (Figure 4.6), the exact values are not as similar as in the case U=3.5.

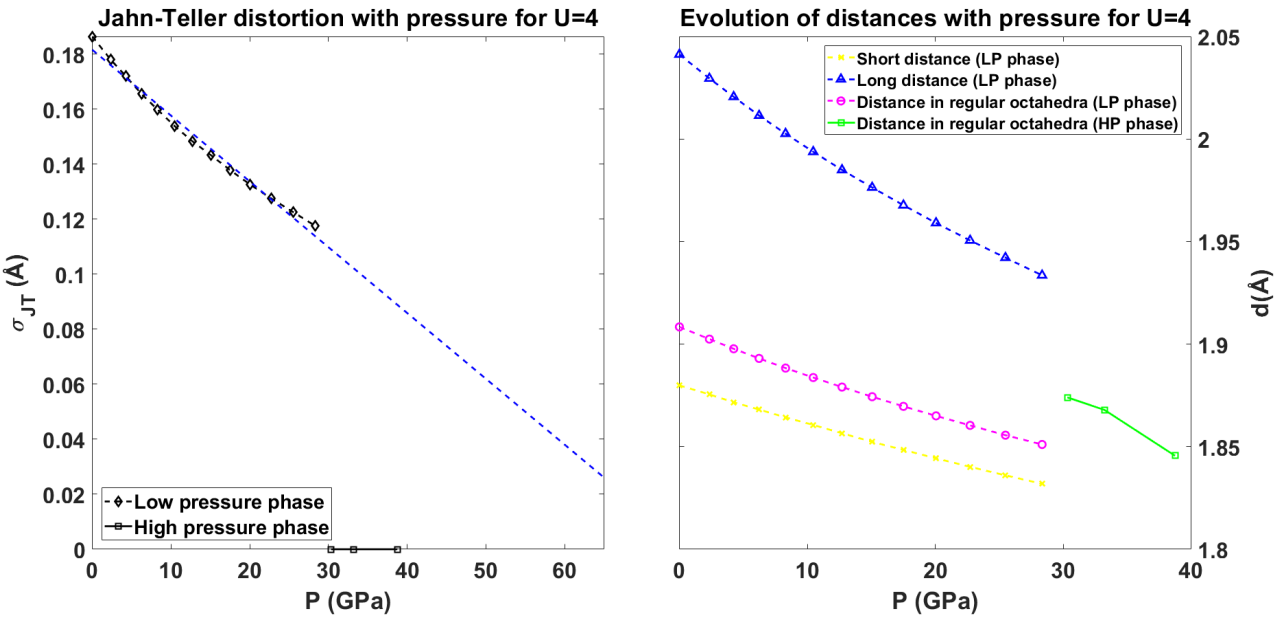

Figure 6.7: (Left) Evolution of the Jahn-Teller distortion with pressure. The dashed line shows a linear extrapolation. The fit is done to the points of the low pressure phase.
(Right) Evolution of the distances in the different types of Mn-O_6 octahedra.

Another feature that is not consistent is the slight increase in the slope between the last two points of the low pressure phase. As it happens for U=3.5 (Figure 5.8 left), the Jahn-Teller distortion should decrease more and more as pressure increases.

The evolution of the distances (Figure 6.7 right) has a subtle qualitative difference with the U=3.5 case. The case U=4 does not reproduce the slight change in the slope of the curves in the range of 25-30 GPa as U=3.5 does.

Same thing applies for the evolution of the volumes of the Mn-O_6 octahedra (Figure 6.8). The values are close to those for U=3.5 (Figure 5.9) and the experimental ones (Figure 4.7) but the change in slope is not seen in this case. The fitting parameters obtained are very close to those obtained for U=3.5. As it happened before, for the fit of the Mn^{3+}- O_6 octahedra, the values of K_0 and K_0' are consistent with the ones in figure 4.7. V_0 is not since it lies out of the error interval but it is very close to the experimental one. This is how it goes for the Mn^{4+}- O_6 octahedra as well.

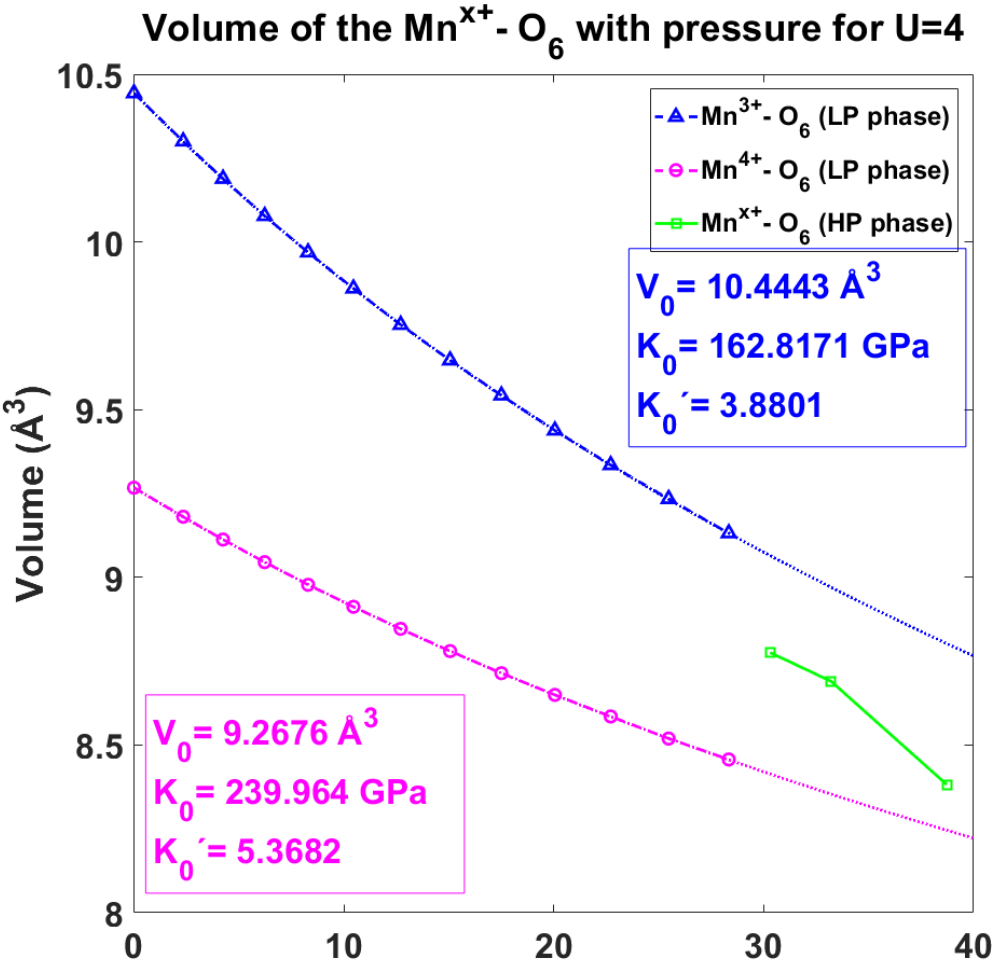

Figure 6.8: Evolution of the volume of the different types of octahedra with pressure. For the octahedra of the low pressure phase, there are fits to a third order Birch-Murnaghan equation considering those points below 20 GPa. The fit parameters are shown in the figure. The octahedra of the high pressure phase are labeled as Mn^{x+}- O_6 due to the fact that the charge-ordering phase transition changes the charge of the Mn at the octahedra.

The long-range structure was almost unaffected by the change from U=3.5 to U=4. Nevertheless, the short-range structure exhibits more differences as we have seen with the behaviour of the slopes and the slight different values of the magnitudes with respect to the U=3.5 case.

Even though the future seems far away, it is actually beginning right now.

Mattie Stepanek

Chapter 7

Conclusions

By carrying out this work, I have had a first contact with DFT calculations and everything that entails.

Firstly, I have learnt how to launch and manage calculations. As a student, I thought running calculations was a thing of launching and leaving until it ends. The reality is that it is not usually like that. You have to check that calculations are still running as expected, relaunch them if necessary, check that queues for calculations are available, that the outputs you get are sensible, running several cases at the same time etc. What I found out is that you have to put your time on it the same way you would do in a laboratory.

I also got a clear picture about how to prepare DFT calculations to obtain structural information. Before getting results, you have to make sure that you are simulating the system realistically. To do so, you have to find an appropiate *k*-point mesh and energy cutoff. Equally, you have to find those parameters that allow you to perform a realistic simulation. In our case, it was the U *Hubbard parameter*. We found the U value that yielded a realistic electronic structure. By finding that U, we could be sure that the structural data we got with further calculations corresponded to a realistic system.

And of course, I have learnt and revisited a lot of theoretical content, and it has been equally rewarding and enjoyable.

In regards to the actual results, we have managed to find that U=3.5 as the *Hubbard parameter* is capable of properly describing the electronic structure. With the band structure and the DOS, we have checked how the value of U heavily influences the electronic structure. We also found out that for U=3.5, the structural properties are reproduced in excellent agreement with experimental data. This supports our statement that a good description of the electronic structure leads to a good description of the local structure.

The energy band gap was found to be indirect with a value of 236.9 meV in good agreement with published data. We also found that the band gap corresponded to a dipole allowed transition between the $2p$ oxygen states and the $3d$ manganese states.

For U=3.5, the start of the phase transition was found to be around 20 GPa, in good agreement with resistivity measurements. We showed that all distances converged to a single one after the phase transition. Simultaneously, the Jahn-Teller distortion vanished at around 28 GPa. These facts are consistent with the expected phase transition from space group $R\bar{3}$ to $Im\bar{3}$. Our results were quantitatively and qualitatively consistent with experimental results. Even the subtle trends of the magnitudes were replicated with our results.

For all the values different than U=3.5, we found a poor or less good agreement with published data. In particular, U=3 did not even reproduce the correct pressure for the phase transition. On the other hand, U=4 was capable of giving good quantitative results, but the details of the trends of the

magnitudes under pressure were not properly reproduced.

References

[1] VASP:About. (2022). Retrieved 21 June 2022, from https://www.vasp.at/info/about/

[2] Stekiel, M., Girard, A., Zimmer, D., Monteseguro, V., Glazyrin, K., & de Pedro, I. et al. (2022). Pressure-induced charge ordering transition in $CaMn_7O_{12}$. *Physical Review B, 105*(6). doi: 10.1103/physrevb.105.064110

[3] Martin, R. (2004). Electronic Structure. doi: 10.1017/cbo9780511805769

[4] Taylor & Francis Group, LLC. (2016). *An Introduction to High-Pressure Science and Technology.*

[5] Hohenberg, P., & Kohn, W. (1964). Inhomogeneous Electron Gas. *Physical Review, 136*(3B), B864-B871. doi: 10.1103/physrev.136.b864

[6] Kohn, W., & Sham, L. (1965). Self-Consistent Equations Including Exchange and Correlation Effects. *Physical Review, 140*(4A), A1133-A1138. doi: 10.1103/physrev.140.a1133

[7] Finocchi, F. (2011). *Density Functional Theory for Beginners Basic Principles and Practical Approaches* lectures notes. Paris: Institut des NanoSciences de Paris (INSP) CNRS and University Pierre et Marie Curie. Retrieved 27 May 2022 from http://www.attaccalite.com/wp-content/uploads/2017/04/pdf_DFT4beginners.pdf

[8] Kaxiras, E. (2003). *Atomic and electronic structure of solids* (1st ed.). Cambridge: Cambridge Univ. Press.

[9] Toulouse, J. (2019). *Introduction to density-functional theory* lectures notes. Paris: Laboratoire de Chimie Théorique Sorbonne Université. Retrieved 27 May 2022 from https://www.lct.jussieu.fr/pagesperso/toulouse/enseignement/introduction_dft.pdf

[10] Perdew, J., & Wang, Y. (1992). Accurate and simple analytic representation of the electron-gas correlation energy. *Physical Review B, 45*(23), 13244-13249. doi: 10.1103/physrevb.45.13244

[11] Tolba, S., Gameel, K., Ali, B., Almossalami, H., & Allam, N. (2018). The DFT+U: Approaches, Accuracy, and Applications. *Density Functional Calculations - Recent Progresses Of Theory And Application.* doi: 10.5772/intechopen.72020

[12] DFT+U: formalism - Vaspwiki. Retrieved 28 May 2022, from https://www.vasp.at/wiki/index.php/DFT%2BU:_formalism

[13] Kirchner-Hall, N., Zhao, W., Xiong, Y., Timrov, I., & Dabo, I. (2021). Extensive Benchmarking of DFT+U Calculations for Predicting Band Gaps. *Applied Sciences, 11*(5), 2395. doi: 10.3390/app11052395

[14] Råsander, Mikael. (2010). *A Theoretical Perspective on the Chemical Bonding and Structure of Transition Metal Carbides and Multilayers.*

[15] Stability of polyatomic molecules in degenerate electronic states - I—Orbital degeneracy. (1937). *Proceedings Of The Royal Society Of London. Series A - Mathematical And Physical Sciences, 161*(905), 220-235. doi: 10.1098/rspa.1937.0142

[16] Fox, M. (2010). *Optical properties of solids*. Oxford: Oxford Univ. Press.

[17] Ghiassi, K., & Lancashire, R. (2020). Jahn-Teller Distortions. Retrieved 21 June 2022, from https://chem.libretexts.org/Bookshelves/Inorganic_Chemistry/Supplemental_Modules_and_Websites_(Inorganic_Chemistry)/Coordination_Chemistry/Structure_and_Nomenclature_of_Coordination_Compounds/Coordination_Numbers_and_Geometry/Jahn-Teller_Distortions

[18] Perdew, J., Ruzsinszky, A., Csonka, G., Vydrov, O., Scuseria, G., & Constantin, L. et al. (2008). Restoring the Density-Gradient Expansion for Exchange in Solids and Surfaces. *Physical Review Letters, 100*(13). doi: 10.1103/physrevlett.100.136406

[19] Huon, A., Lang, A., Saldana-Greco, D., Lim, J., Moon, E., & Rappe, A. et al. (2015). Electronic transition above room temperature in $CaMn_7O_{12}$ films. *Applied Physics Letters, 107*(14), 142901. doi: 10.1063/1.493213210.1063/1.4932132

[20] Lim, J., Saldana-Greco, D., & Rappe, A. (2018). Improper magnetic ferroelectricity of nearly pure electronic nature in helicoidal spiral $CaMn_7O_{12}$. *Physical Review B, 97*(4). doi: 10.1103/physrevb.97.045115

[21] KPOINTS - Vaspwiki. Retrieved 1 June 2022, from https://www.vasp.at/wiki/index.php/KPOINTS

[22] Troyanchuk, I., Lobanovsky, L., Kasper, N., Hervieu, M., Maignan, A., & Michel, C. et al. (1998). Magnetotransport phenomena in $A(Mn_{3-x}Cu_x)\,Mn_4O_{12} (A = Ca, Tb, Tm)$ perovskites *Physical Review B, 58*(22), 14903-14907. doi: 10.1103/physrevb.58.14903

[23] Ruiz-Fuertes, J., Friedrich, A., Pellicer-Porres, J., Errandonea, D., Segura, A., & Morgenroth, W. et al. (2011). Structure Solution of the High-Pressure Phase of $CuWO_4$ and Evolution of the Jahn-Teller Distortion. *Chemistry Of Materials, 23*(18), 4220-4226. doi: 10.1021/cm201592h

[24] Katsura, T., & Tange, Y. (2019). A Simple Derivation of the Birch–Murnaghan Equations of State (EOSs) and Comparison with EOSs Derived from Other Definitions of Finite Strain. *Minerals, 9*(12), 745. doi: 10.3390/min9120745

[25] Aguado, F., Rodríguez, F., Valiente, R., Itiè, J., & Hanfland, M. (2012). Pressure effects on Jahn-Teller distortion in perovskites: The roles of local and bulk compressibilities. *Physical Review B, 85*(10). doi: 10.1103/physrevb.85.100101

[26] Andriyevsky, B., Doll, K., & Jacob, T. (2014). Electronic and transport properties of $LiCoO_2$. *Phys. Chem. Chem. Phys., 16*(42), 23412-23420. doi: 10.1039/c4cp03052d

[27] Das, S., Bhuyan, M., & Basith, M. (2021). First-principles calculation of the electronic and optical properties of Gd_2FeCrO_6 double perovskite: Effect of Hubbard U parameter. *Journal Of Materials Research And Technology, 13*, 2408-2418. doi: 10.1016/j.jmrt.2021.06.026

[28] Cao, K., Johnson, R., Perks, N., Giustino, F., & Radaelli, P. (2015). First-principles study of structurally modulated multiferroic $CaMn_7O_{12}$. *Physical Review B, 91*(6). doi: 10.1103/physrevb.91.064422